JGR Space Physics

RESEARCH ARTICLE
10.1029/2024JA032669

Kinetic Signatures, Dawn-Dusk Asymmetries, and Flux Transfer Events Associated With Mercury's Dayside Magnetopause Reconnection From 3D MHD-AEPIC Simulations

Changkun Li[1], Xianzhe Jia[1], Yuxi Chen[2], Gabor Toth[1], Hongyang Zhou[3], James A. Slavin[1], Weijie Sun[4], and Gangkai Poh[5]

[1]Department of Climate and Space Sciences and Engineering, University of Michigan - Ann Arbor, Ann Arbor, MI, USA, [2]Boston University, Revere, MA, USA, [3]University of Helsinki, Helsinki, Finland, [4]University of California, Berkeley, Berkeley, CA, USA, [5]Planetary Magnetospheres Laboratory, NASA Goddard Space Flight Center, Greenbelt, MD, USA

Key Points:

- A series of 3D MHD-AEPIC simulations are performed to reveal kinetic signatures of Mercury's magnetopause reconnection
- A novel metric and algorithm are developed to identify reconnection sites whose spatial distribution exhibit notable dawn-dusk asymmetries
- Flux transfer events in our simulations carry a large amount of open flux contributing up to 36% of the total flux opened at the dayside

Correspondence to:

C. Li and X. Jia,
changkul@umich.edu;
xzjia@umich.edu

Citation:

Li, C., Jia, X., Chen, Y., Toth, G., Zhou, H., Slavin, J. A., et al. (2024). Kinetic signatures, dawn-dusk asymmetries, and flux transfer events associated with Mercury's dayside magnetopause reconnection from 3D MHD-AEPIC simulations. *Journal of Geophysical Research: Space Physics*, *129*, e2024JA032669. https://doi.org/10.1029/2024JA032669

Received 24 MAR 2024
Accepted 24 MAY 2024

Abstract Mercury possesses a miniature yet dynamic magnetosphere driven primarily by magnetic reconnection occurring regularly at the magnetopause and in the magnetotail. Using the newly developed Magnetohydrodynamics with Adaptively Embedded Particle-in-Cell (MHD-AEPIC) model coupled with planetary interior, we have performed a series of global simulations with a range of upstream conditions to study in detail the kinetic signatures, asymmetries, and flux transfer events (FTEs) associated with Mercury's dayside magnetopause reconnection. By treating both ions and electrons kinetically, the embedded PIC model reveals crescent-shaped phase-space distributions near reconnection sites, counter-streaming ion populations in the cusp region, and temperature anisotropies within FTEs. A novel metric and algorithm are developed to automatically identify reconnection X-lines in our 3D simulations. The spatial distribution of reconnection sites as modeled by the PIC code exhibits notable dawn-dusk asymmetries, likely due to such kinetic effects as X-line spreading and Hall effects. Across all simulations, simulated FTEs occur quasi-periodically every 4–9 s. The properties of simulated FTEs show clear dependencies on the upstream solar wind Alfvénic Mach number (M_A) and the interplanetary magnetic field orientation, consistent with MESSENGER observations and previous Hall-MHD simulations. FTEs formed in our MHD-AEPIC model tend to carry a large amount of open flux, contributing ~3%–36% of the total open flux generated at the dayside. Taken together, our MHD-AEPIC simulations provide new insights into the kinetic processes associated with Mercury's magnetopause reconnection that should prove useful for interpreting spacecraft observations, such as those from MESSENGER and BepiColombo.

1. Introduction

In situ measurements obtained from the Mercury Surface, Space Environment, Geochemistry and Ranging (MESSENGER) spacecraft revealed that Mercury's intrinsic magnetic field can be well represented as a dipole aligned with the planetary rotation axis with an equatorial surface strength of 195 nT and a northward offset of 0.2 R_M (Anderson et al., 2008, 2011). The interaction of Mercury's intrinsic field with the inner heliosphere solar wind forms a magnetosphere around the planet, whose overall structure is similar to Earth's in that it features a bow shock upstream to the magnetopause, cusp regions at the dayside high latitudes, and an elongated magnetotail with a central plasma sheet (Slavin et al., 2008; Zurbuchen et al., 2011). Due to the relatively weak intrinsic magnetic field and the highly variable solar wind conditions at Mercury's orbit, Mercury possesses an extremely dynamic magnetosphere which is primarily driven by the solar wind through magnetic reconnection (Slavin & Holzer, 1979). Extensive research efforts have been dedicated to the study of reconnection-driven dynamics in Mercury's magnetosphere. For instance, Slavin et al. (2009), Slavin, Anderson, et al. (2010), and DiBraccio et al. (2013) found that Mercury's intrinsic field can reconnect with shocked interplanetary magnetic field (IMF) under a wide range of magnetic shear angles. Slavin, Anderson, et al. (2010) observed that the Dungey cycle at Mercury occurs on a timescale of the order of a couple of minutes, considerably shorter than the typical duration of ~60 min at Earth (Baker et al., 1996). Such a rapid Dungey-cycle has been attributed to the frequent occurrence of magnetopause reconnection and the compact size of Mercury's magnetosphere.

One of the prominent features of magnetopause reconnection is the formation of flux transfer events (FTEs), which were first observed at the Earth's magnetopause (Russell & Elphic, 1978). Notable characteristics of FTEs include their bipolar variations in the normal component of the magnetic field with respect to the magnetopause surface and enhanced field strength near their centers. These magnetic signatures associated with FTEs suggest that their interior structures largely resemble flux ropes with helical topology. Following the discovery of FTEs, various formation mechanisms have been proposed to account for the observed magnetic signatures (see a recent review by Hwang et al., 2023), including localized, bursty reconnection (e.g., Russell & Elphic, 1978), multiple X-line reconnection (Lee & Fu, 1985), and single X-line reconnection with time-varying reconnection rates (Scholer, 1988; Southwood et al., 1988). Extensive observations from MESSENGER have revealed that FTEs form frequently at Mercury with a time separation of only a few seconds between consecutive FTEs (Slavin et al., 2012), much shorter than the typical time separation observed for FTEs at Earth (Rijnbeek et al., 1984; Russell et al., 1996). As a result of their frequent occurrence, FTEs are considered to play a significant role in driving Mercury's Dungey cycle (Slavin, Anderson, et al., 2010). Numerous studies based on MESSENGER in-situ observations have been conducted to examine the significance of FTEs in driving Mercury's global magnetospheric convection. Specifically, a case study by Imber et al. (2014) inferred that large-size FTEs observed by MESSENGER could contribute at least 30% of the open flux required to drive the substorm cycle at Mercury. By analyzing the MESSENGER data collected during FTE shower events, Sun et al. (2020) estimated that during FTE shower intervals, approximately 60%–85% of the magnetic flux opened at Mercury's dayside magnetopause could be carried by FTEs. Motivated by studies of Earth's FTEs, Fear et al. (2019) suggested that FTEs at Mercury may make an even greater contribution to the open flux generation if the magnetic flux contained in the post-FTE reconnection exhaust is also taken into consideration. Complementing observational studies that do not provide global context due to limited spatial coverage, Li et al. (2023) recently conducted a series of global Hall-magnetohydrodynamics (MHD) simulations of Mercury's magnetosphere to study the characteristics of FTEs and reported that the overall contribution by FTEs to open flux generation at the day side varies from 3% to 13% for different input solar wind and IMF conditions. However, it is worth noting that the Hall-MHD model used in the previous work includes the Hall effect by allowing separate bulk motions of ions and electrons, but it treats both plasma ions and electrons as fluids. Therefore, it could not fully capture the behavior of plasma at kinetic scales, especially in regions where kinetic effects play an important role, such as near reconnection sites.

In order to study plasma phenomena in Mercury's magnetosphere involving kinetic processes, such as magnetic reconnection and formation of FTEs, a numerical model that incorporates kinetic physics is required. To that end, hybrid models, which consider ions as kinetic particles and electrons as a fluid, have been employed to simulate the interaction between solar wind and Mercury's magnetosphere (e.g., Exner et al., 2018; Fatemi et al., 2018; Lu et al., 2022; Müller et al., 2012; Trávnícek et al., 2010). However, because electrons are still modeled as a fluid in hybrid simulations, they lack electron kinetic physics, which is believed to play an important role in reconnection physics. In contrast, Particle-in-Cell (PIC) codes treat both ions and electrons as interacting kinetic particles, thereby allowing for a more accurate description of kinetic processes, including electron-scale dynamics. Coupled fluid-PIC (Y. Chen et al., 2019) and pure semi-implicit PIC (Lapenta et al., 2022; Lavorenti et al., 2022) simulations have been conducted previously to study the large-scale configuration and global-scale dynamics of Mercury's magnetosphere. However, there have not been dedicated simulation efforts based on a kinetic modeling approach devoted to understanding the occurrence and kinetic signatures of Mercury's magnetopause reconnection, as well as the impact of kinetic physics on the formation and evolution of FTEs.

Inspired by the previous coupled fluid-PIC simulations performed by Y. Chen et al. (2019), where a rectangular PIC box was placed near the tail plasma sheet to model reconnection-driven dynamics in Mercury's magnetotail, here we use the newly developed Magnetohydrodynamics with Adaptively Embedded Particle-in-Cell (MHD-AEPIC) model (Y. Chen et al., 2023; Shou et al., 2021; X. Wang et al., 2022) to simulate Mercury's magnetosphere under various solar wind and IMF conditions with a focus on the kinetic signatures, asymmetries, and FTEs associated with the reconnection at Mercury's dayside magnetopause. Recent advances in model development and computational capability allow us to place a non-rectangular PIC region with high-resolution grid to cover the entire dayside magnetopause such that we can resolve the kinetic physics on a scale comparable to the electron skin depth and study the reconnection process from a kinetic perspective. Insights into the effects of kinetic physics on FTE characteristics and global magnetospheric dynamics can also be obtained by comparing the results from MHD-AEPIC with our previous Hall-MHD simulations (Li et al., 2023).

In the work presented here, we define "FTEs" as flux ropes formed on the magnetopause with one end connected to the IMF and the other connected to Mercury. Therefore, the physical properties of FTEs that we examine below, such as the magnetic flux content and spatial size, all correspond to those of the flux ropes associated with FTEs. As we will show later on, FTEs in our simulations are formed primarily as a result of multiple X-line reconnection, as proposed by Lee and Fu (1985). However, the regions between individual flux ropes may still be filled with additional open magnetic flux produced by magnetopause reconnection (Fear et al., 2019). The total flux opened by dayside magnetopause reconnection is, therefore, the sum of all these sources (e.g., Sun et al., 2020), which we also analyze in assessing the role of FTEs in open flux generation.

The structure of this paper is as follows: Section 2 provides a detailed description of our numerical model, simulation setup, and input parameters. In Section 3, we present the kinetic signatures associated with dayside magnetopause reconnection and introduce a novel metric and algorithm developed for automatic identification of reconnection sites in our MHD-AEPIC simulations. Furthermore, we present the asymmetries in reconnection occurrence and properties of simulated FTEs in Section 3 and conduct a detailed discussion of these results in Section 4. Finally, Section 5 presents a summary of our work with concluding remarks.

2. Methodology

The coupled fluid-kinetic model, MHD-EPIC (MHD with Embedded Particle-in-Cell), has been successfully applied to investigate the interaction between Jupiter's magnetospheric plasma and Ganymede's magnetosphere (Tóth et al., 2016; Zhou et al., 2019, 2020), Mercury's magnetotail reconnection (Y. Chen et al., 2019), and Earth's dayside reconnection-driven dynamics (Y. Chen et al., 2017). The Mercury simulations presented in this paper were performed with the newly developed MHD-AEPIC model (X. Wang et al., 2022). The global magnetosphere is simulated by the BATSRUS Hall-MHD model (Powell et al., 1999; Tóth et al., 2008), and the entire dayside magnetopause is covered by a semi-implicit, particle-in-cell code (PIC) called Flexible Exascale Kinetic Simulator (FLEKS, Y. Chen et al., 2023), which allows for a proper treatment of the kinetic effects of magnetic reconnection. The MHD and FLEKS models are two-way coupled (Daldorff et al., 2014) through the Space Weather Modeling Framework (SWMF) (Gombosi et al., 2021; Tóth et al., 2012) by exchanging information periodically at prescribed temporal frequency. For all the simulations conducted for this work, we first ran the BATSRUS Hall-MHD model in local time stepping mode to establish a quasi steady-state magnetosphere, and then switch to time-accurate mode and start the coupling between the MHD and PIC codes. The simulation setup for both BATSRUS and FLEKS are described in the following subsections.

2.1. Global Hall-MHD Model: BATSRUS

The Mercury MHD model used in this work is based on the work of Jia et al. (2015), who adapted BATSRUS to Mercury by modeling the planet as a resistive body consisting of a perfectly conducting core of radius 0.8 R_M (R_M = 2,440 km is Mercury's mean radius) surrounded by a highly resistive mantle (between 0.8 R_M and 1 R_M). The resistivity profile used in our MHD-AEPIC simulations is identical to that used in Jia et al. (2015, 2019). To account for the induction effect of Mercury's conducting core, a zero magnetic field perturbation boundary condition is applied at the core-mantle boundary (0.8 R_M), whereas boundary conditions for other MHD primitive variables (plasma density, velocity, and pressure) are prescribed at Mercury's surface (1 R_M). Inside the planet, only a reduced Faraday's law (Equation 1) is solved to model the diffusion of the magnetic field through Mercury's interior.

$$\frac{\partial \boldsymbol{B}}{\partial t} = -\nabla \times (\eta \boldsymbol{J}), \tag{1}$$

where $\boldsymbol{B}$ is the magnetic field vector, $\boldsymbol{J}$ denotes the current density and η is the resistivity prescribed according to Jia et al. (2015, 2019). Mercury's internal magnetic field is represented in the simulation as a dipole aligned with the planet's rotation axis with an equatorial surface strength of 195 nT and a northward offset of 0.2 R_M, according to MESSENGER results (Anderson et al., 2011).

The BATSRUS Hall MHD model used in this work includes a separate equation for the electron pressure, as well as the corresponding electron pressure gradient term in the generalized Ohm's law used to advance the induction equation for the magnetic field. The set of Hall-MHD equations and the layered inner boundary conditions are

described in detail in Li et al. (2023). A semi-implicit scheme (Tóth et al., 2012), which relaxes the stiffness arising from the Hall term and the resistivity term without limiting the timestep, is used to reduce the computational costs.

The simulations are performed in MSO (Mercury Solar Orbital) coordinates, where the $+X$-axis is pointing from Mercury to the Sun, the $+Z$-axis is perpendicular to Mercury's equatorial plane and is pointing northward, and the Y-axis completes the right-handed system with positive pointing in the direction opposite to Mercury's orbital motion. The entire simulation domain is a rectangular box with dimensions of $-64\ R_M < X < 8\ R_M$, $-128\ R_M < Y < 128\ R_M$, $-128\ R_M < Z < 128\ R_M$ cut out of a spherical grid. A scaling/Hall factor (Tóth et al., 2017) of 4, which was shown to work reasonably well in our previous global Hall MHD simulations (Li et al., 2023), is used to scale up the kinetic length by a factor of 4 by artificially increasing the ion mass-to-charge ratio. A stretched spherical grid with up to three levels of adaptive mesh refinement near the dayside magnetopause is used for all simulations, resulting in a grid resolution of 20 km or 0.008 R_M, which is equal to 1/6 of the ion inertial length after scaling. Figure 1a shows the structure of the numerical grid in the XZ plane with the background colors representing the plasma density contours.

The outer boundary conditions at the six faces of the simulation box are set as follows. At the upstream face, an inflow boundary condition is imposed to allow the solar wind with prescribed parameters to flow into the simulation domain. For the other five faces, we have used a zero-gradient floating boundary condition such that the super-magnetosonic plasma flow can leave the simulation domain freely.

In total, we have conducted six MHD-AEPIC simulations with different solar wind and IMF conditions (see Table 1). We note that the IMF clock angle used in this work is defined as the angle between the IMF vector projected onto the YZ plane and the $+Z$ axis of MSO coordinates, and it increases counter-clockwise as viewed from the direction of the solar wind flow (i.e., 90° corresponds to IMF along the $-Y$-axis and 270° corresponds to the $+Y$-axis). The upstream conditions used in this paper are the same as those used in Li et al. (2023), which allows us to make direct comparisons of simulation results between the coupled fluid-kinetic model and the Hall MHD model. It should pointed out that, in order to ease the analysis of our simulation results, we have assumed zero radial component (or x-component in MSO coordinates) for the IMF in the two sets of simulations, whereas the IMF observed at Mercury's orbit typically has a significant radial component, which would potentially lead to additional north-south asymmetries in the magnetospheric configuration.

2.2. PIC Model: FLEKS

FLEKS is a semi-implicit, particle-in-cell (PIC) code developed by Y. Chen et al. (2023). It uses Gauss's law satisfying energy-conserving semi-implicit method (GL-ECSIM) (Y. Chen & Tóth, 2019) to resolve the kinetic physics in the PIC domain. FLEKS employs an adaptive Cartesian grid which allows changing the simulation domain dynamically by turning on and off selected computational cells. In this work, we have used an active PIC region that is fixed in time to cover the entire dayside magnetopause. The PIC box has a uniform mesh covering the region between $0 < X < 2\ R_M$, $-2.25\ R_M < Y < 2.25\ R_M$, and $-2\ R_M < Z < 2\ R_M$ with a grid resolution of 1/96 R_M in all directions. As shown in Figures 1b and 1c, the inner and outer boundaries of the active PIC region are prescribed by two elliptic paraboloids. The nose of the PIC inner boundary is placed in the $Z = 0\ R_M$ plane for the $M_A = 6$ simulations (Runs #1, #2, #3) and in the $Z = 0.05\ R_M$ plane for the $M_A = 2$ simulations (Runs #4, #5, #6). We have shifted the inner boundary of the PIC domain for the $M_A = 2$ simulations slightly northward to avoid statistical noise caused by small electron pressure values near Mercury's surface. The nose of the PIC outer boundary is placed in the $Z = 0\ R_M$ plane for all simulations. Sixty-four macroparticles per cell per particle species are used to initialize the active PIC region. To reduce the computational cost and make the simulations affordable, we have assumed the proton-to-electron mass ratio (m_p/m_e) to be 100 and artificially reduced the speed of light (c) by an order of magnitude to 30,000 km/s, which is still 10 times larger than the reconnection electron jet speed.

The PIC grid resolution of 1/96 R_M is about 1/5 of the ion inertial length and twice the electron skin depth after applying the scaling factor of 4 (see Section 2.1) and the artificially reduced proton-electron mass ratio of 100. Although such choice of cell size cannot fully resolve the electron-scale physics, it was proven to work reasonably well in producing the correct reconnection rate, reconnection outflows, and the Hall magnetic field (Y. Chen & Tóth, 2019). Our test results also suggest that a grid resolution of 1/96 R_M achieves a desired balance between computational cost and the need for resolving kinetic scales.

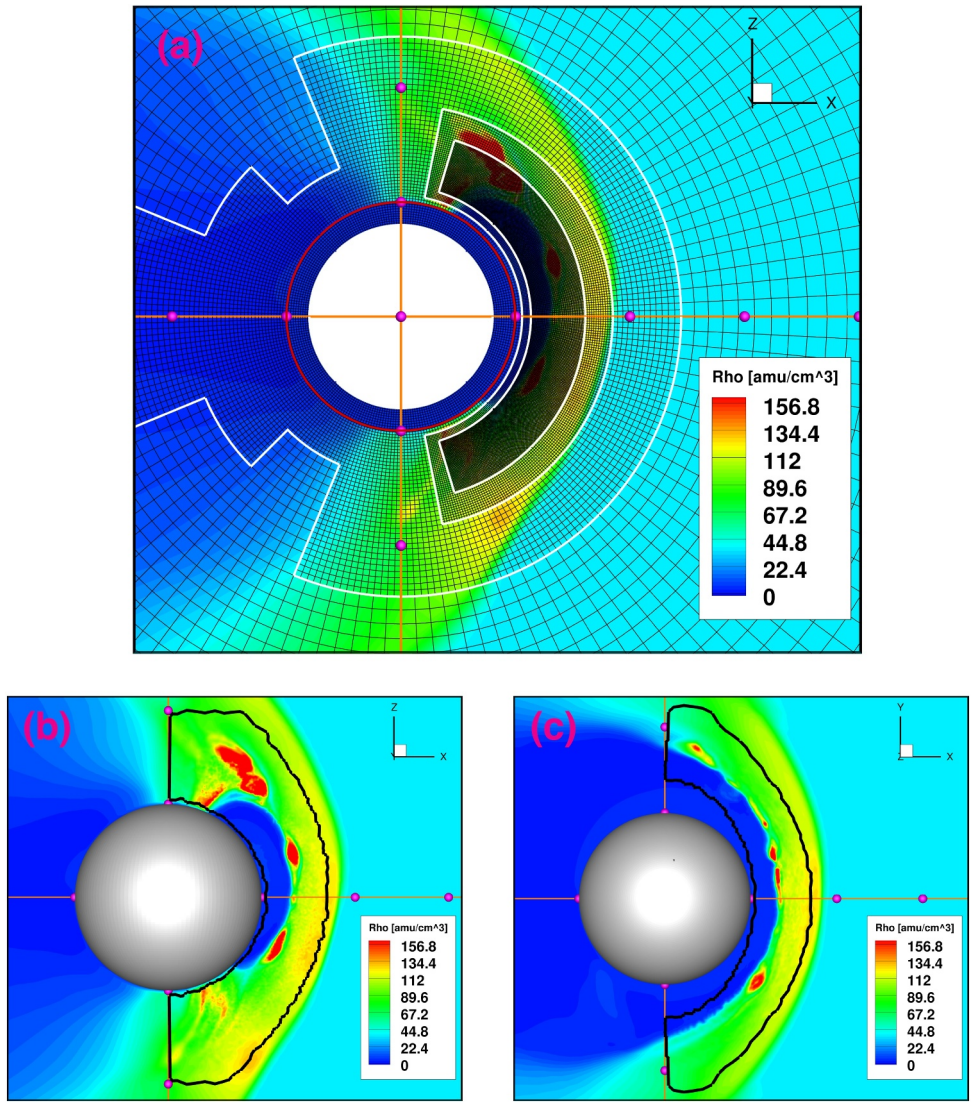

Figure 1. The structure of the BATSRUS Hall-MHD grid and the active PIC region. (a) Stretched spherical grid (in black) used by the BATSRUS Hall-MHD model with three levels of adaptive mesh refinement (AMR) at the dayside magnetopause, as viewed in the *XZ* plane. The boundaries between successive AMR levels are indicated by the white curves. The red circle centered at the origin with radius of 1 R_M represents the surface of Mercury and the centered white-filled disk represents Mercury's conducting core with an assumed radius of 0.8 R_M. (b) and (c) The boundaries of the active PIC region (marked by the black curves) in the *XZ* and *XY* planes, respectively. Mercury is represented by a gray sphere with a radius of 1 R_M in the center. The background colors in all panels show the plasma density (ρ) contours. For illustration purposes, the density contours were extracted from Run #1 ($M_A = 6$, interplanetary magnetic field clock angle = 180°) and the distance between neighboring magenta balls on the axes is 1 R_M.

2.3. Coupling Between BATSRUS and FLEKS

BATSRUS and FLEKS are coupled through the SWMF (Gombosi et al., 2021; Tóth et al., 2012). Both models run simultaneously with different time steps and they are set to exchange information every 0.01 s for all of the six MHD-AEPIC simulations that we have performed. At $T = 0$ s, FLEKS assumes a Maxwellian distribution in initializing the macro particles according to the plasma bulk properties (i.e., plasma density, bulk flow velocity, and temperature) from the Hall MHD that has been run in localtime stepping model to reach a quasi-steady state magnetosphere. A coupler is employed to handle the interpolation and communication of variables between the two models. At the coupling timestep, FLEKS overwrites the Hall-MHD solution with the PIC results in the active region of the PIC code, and takes the latest information (e.g., plasma bulk properties and the magnetic field)

Table 1
Solar Wind and Interplanetary Magnetic Field Parameters for the Simulations Presented in This Study

Run #	M_A	B	IMF clock angle (°)	B_y (nT)	B_z (nT)	U_x (km/s)	ρ (amu/cc)	T (K)
1	6	0.2	180	0	−23	−500	36	8.7e4
2	6	0.2	135	−16	−16	−500	36	8.7e4
3	6	0.2	90	−23	0	−500	36	8.7e4
4	2	0.02	180	0	−69	−500	36	8.7e4
5	2	0.02	135	−49	−49	−500	36	8.7e4
6	2	0.02	90	−69	0	−500	36	8.7e4

from the BATSRUS Hall-MHD code to set the boundary conditions for the PIC model. Then, the two models advance individually with their own timesteps until reaching the next coupling time. For the simulations presented here, the MHD-AEPIC model was run for 200 s in physical time, which is comparable to the typical timescale of Mercury's Dungey cycle, resulting in a total of 20,000 couplings between BATSRUS and FLEKS.

3. Simulation Analysis and Results

In this section, we present the results of our simulations for different upstream conditions listed in Table 1, with a focus on the kinetic signatures and asymmetries associated with the dayside magnetopause reconnection and the properties of FTEs. Section 3.1 discusses the reconnection-driven kinetic signatures of ion and electron distributions modeled by PIC. Section 3.2 describes the metric and algorithm we have developed to automatically identify the reconnection sites in our simulations. Section 3.3 presents dawn-dusk asymmetries in the distribution of identified reconnection sites and the associated non-ideal electric fields as predicted by our MHD-AEPIC model. Lastly, in Section 3.4, we provide a statistical survey of key properties of FTEs simulated by PIC, which are compared to the results from our previous work based on Hall-MHD simulations.

3.1. Kinetic Signatures Associated With Mercury's Magnetopause Reconnection as Simulated by PIC

Since the PIC model, FLEKS, uses a grid resolution comparable to the electron skin depth, we can directly investigate the kinetic signatures of ions and electrons associated with dayside magnetopause reconnection by studying their phase space distributions. To facilitate interpretation of the simulation results, we present the velocity distributions of ions and electrons in a field-aligned coordinate system constructed based on the ambient magnetic field (**B**) and plasma bulk flow (**U**) directions. Specifically, $V_{//}$ denotes the component of the particle velocity parallel to the local magnetic field, $V_{\mathbf{B}\times\mathbf{U}}$ represents the component parallel to $\mathbf{B}\times\mathbf{U}$, and V_{perp} completes the right-handed system.

Figure 2 shows selected ion and electron phase space distribution functions on the magnetosheath side of a reconnection site from Run #4 ($M_A = 2$, IMF clock angle = 180°). Both the ion and electron distributions were extracted from a sphere centered at $X = 1.2\ R_M$, $Y = 0\ R_M$, $Z = 0.8\ R_M$ with a radius of $0.05\ R_M$. As shown in Figure 2d, the ion phase space distribution exhibits a clear crescent-like shape in the plane perpendicular to the local magnetic field. The electron distribution in the same plane, depicted in Figure 2g, also exhibits a crescent-shaped pattern, albeit with less prominent signature compared to the ion distribution. We have also checked the ion and electron distributions on the magnetospheric side of the same reconnection site, but found no crescent-like distributions for both species. The result that crescent-shaped distributions are found on the magnetosheath side of the reconnection site in our simulations contrasts with the observations from the Magnetospheric Multiscale (MMS) mission at the Earth's magnetopause (Burch et al., 2016) and previous MHD-EPIC simulations of Ganymede's magnetopause reconnection (Zhou et al., 2019), where crescent-shaped distributions were found to form predominantly on the magnetospheric side due to the meandering motion of magnetosheath particles through the diffusion region (e.g., Bessho et al., 2017; Hesse et al., 2014; Lapenta et al., 2017; Shay et al., 2016). However, it is worth noting that charged particles can also undergo meandering motion in regions containing thin current sheets, where their gyroradii may become comparable to or even larger than the minimum radius of curvature of the magnetic field lines (e.g., Buchner & Zelenyi, 1989; J. Chen & Palmadesso, 1986). As a result, crescent-shaped distributions have been found at Earth not only in the vicinity of the diffusion region but also in the reconnection exhaust (e.g., Artemyev et al., 2010; Lottermoser et al., 1998; S. Wang et al., 2014). The

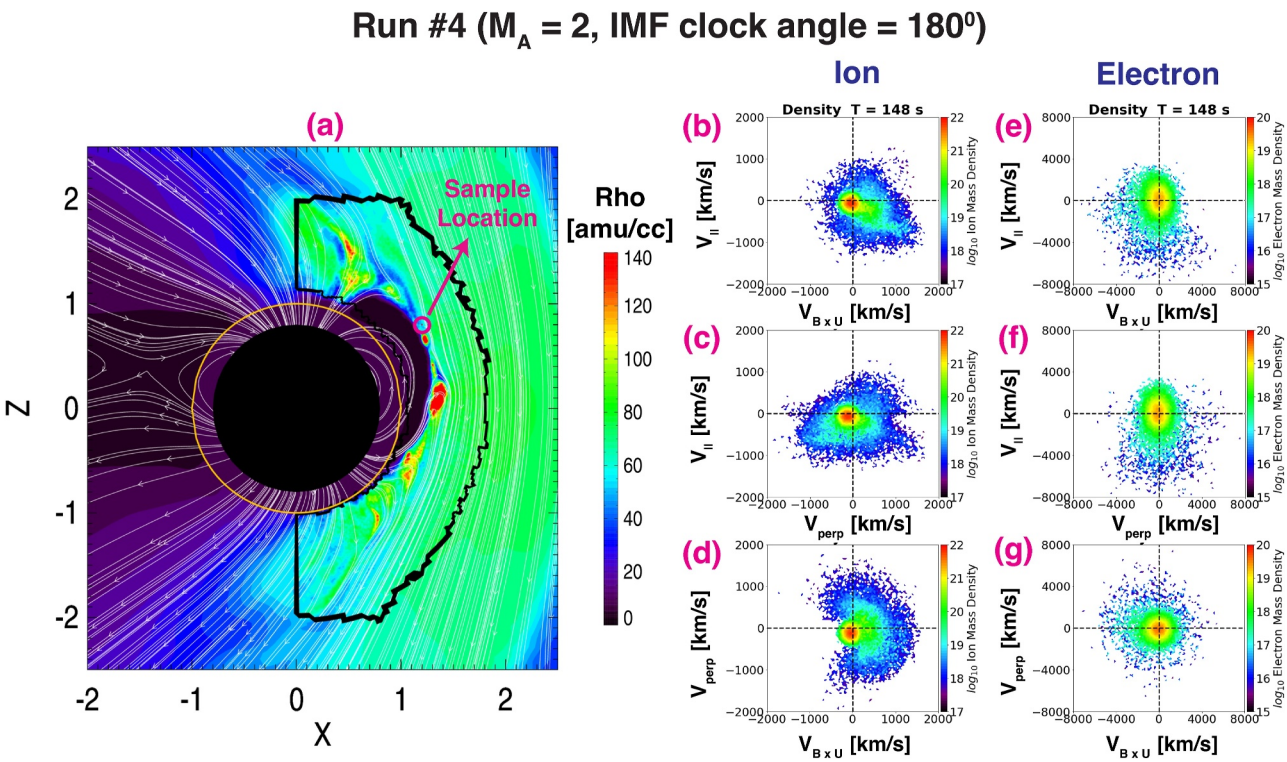

Figure 2. Ion and electron phase space distributions in logarithmic scale on the magnetosheath side of a reconnection site from Run #4 at T = 148 s. (a) Contours of plasma density in the XZ plane with sample magnetic field lines overplotted as white arrowed lines showing the global configuration of the simulated magnetosphere. The yellow circle with radius 1 R_M shows Mercury's surface and the black-filled disk with radius 0.8 R_M represents its conducting core. The black curve marks the boundary of the active PIC region. The magenta circle near the magnetopause boundary indicates the sampling location used to extract the ion and electron phase space distributions. Panels (b)–(d) and (e)–(g) show the phase space distributions for ions and electrons, respectively. The distributions are displayed in a field-aligned coordinate system with the parallel direction along the ambient magnetic field (**B**), one perpendicular direction along the direction of **B** × **U** (**U** is the plasma bulk flow velocity) and the other perpendicular direction completing the right-handed system. The unit of phase space density is amu*s^2/km^2.

distribution functions shown in Figure 2 were extracted from a sphere located on the magnetosheath side of the reconnection X-line that also includes a significant portion of the reconnection outflow region. Therefore, it is likely that the crescent-shaped distributions seen in our case are associated with reconnection outflows carrying reconnected field lines away from the diffusion region.

In addition to the crescent-shaped distribution, the electron phase space distributions exhibit preferential heating along the magnetic field direction, which is approximately aligned with the reconnection outflow direction at the sampling location shown here. Such heating results in notable temperature anisotropies, which are evident from the elongated shapes in the distributions shown in Figures 2e and 2f. In contrast, such temperature anisotropy is not observed in the ion distributions, possibly due to their larger mass compared to electrons. Within the sampling region, the cross product of the magnetic field and the plasma bulk velocity directions (**B** × **U**) is roughly along $+Y$ direction pointing to the dusk side. As shown in Figures 2b and 2e, the ions and electrons exhibit drifts toward the duskside and dawnside, respectively, which are consistent with the direction of the into-the-plane magnetopause currents (in $+Y$ direction in MSO coordinates).

Figure 3 shows the phase space distributions for ions and electrons sampled in the mid-latitude southern cusp region from the same run as shown in Figure 2 (Run #4), but at a different time (T = 65 s). The sampling region is a sphere with radius of 0.05 R_M centered at X = 0.85 R_M, Y = 0 R_M, Z = −0.8 R_M (Figure 3a). As shown in Figures 3b and 3c, the ion phase space distributions exhibit a clear signature of counter-streaming particle populations, characterized by the presence of two groups of particles traveling along the parallel (radially outward) and anti-parallel (radially inward) directions relative to the local magnetic field. In contrast, the electrons show a Maxwellian-like distribution in all three planes, and do not

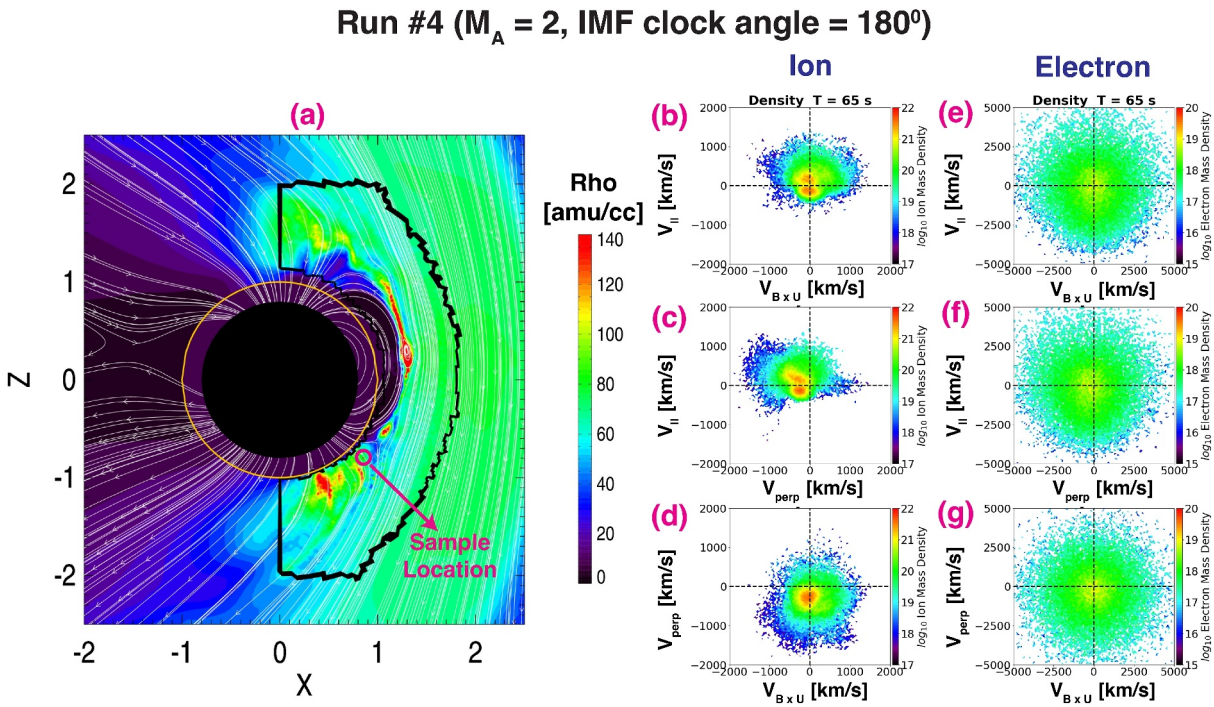

Figure 3. Same as Figure 2 but for a sampling location positioned in the southern cusp region at $X = 0.85\ R_M$, $Y = 0\ R_M$, $Z = -0.8\ R_M$. The ion and electron distributions were extracted from Run #4 at $T = 65$ s. Counter-streaming ion distribution associated with precipitating and mirrored particles in the cusp can be clearly seen in panels (b) and (c).

display a similar counter-streaming signature. The direction of the plasma bulk velocity in the vicinity of Mercury's surface within the southern cusp region around $T = 65$ s is pointing radially inward, suggesting that no appreciable amount of plasma is outflowing from the surface into the magnetosphere at this time. Therefore, the outgoing ions seen in panes (b) and (c) correspond to particles that are reflected at mirror points above the planetary surface within the cusp region. Both the precipitating and mirrored particles originate from the magnetopause, where reconnection accelerates particles to speeds of hundreds of km/s traveling along the field line into the cusp region. A fraction of those precipitating particles (with pitch angles outside of the loss cone) are reflected back toward high altitudes due to the mirror force, forming the outgoing ion population seen in the phase-space distribution. The example shown here of counter-streaming ions as a product of magnetopause reconnection provides a prediction that may be testable with in-situ observations from future missions, such as the BepiColombo mission.

Figure 4 presents the ion and electron distribution functions measured by two virtual satellites (S1 and S2) at $T = 119$ s from Run #5 ($M_A = 2$, IMF clock angle = 135°). Both satellites sample the particles within a sphere of radius 0.05 R_M. Satellite S1 is located at $X = 1.15\ R_M$, $Y = 0\ R_M$, $Z = 0.77\ R_M$, which is near the center of an FTE. Within this FTE, both the ion and electron distributions show significant deviations from Maxwellian distribution with notable temperature anisotropies, which are associated with particle heating resulting from magnetic reconnection. Satellite S2 is situated at $X = 0.75\ R_M$, $Y = 0\ R_M$, $Z = -1.0\ R_M$, which is near the southern cusp region. In the plane perpendicular to the magnetic field, both the ion and electron distributions are observed to exhibit crescent-like shape as shown in the bottom plots of Figures 4d and 4e. Close inspection of the magnetic field topology around this time suggests that the virtual satellite S2 is located on the magnetosheath side of a high-latitude X-line. As we discussed earlier for Figure 2, the crescent-shaped distributions seen here are also likely associated with reconnected field lines in the reconnection exhaust. Furthermore, as shown in Figures 4d and 4e, crescent-shaped distributions are also present for both ions and electrons in the other two planes that involve the parallel direction (along $\boldsymbol{B}$), indicating the transition from a perpendicular crescent to a field-aligned flow. This transition serves as strong evidence for the opening of magnetic field lines, as previously suggested by Burch et al. (2016) based on MMS observations.

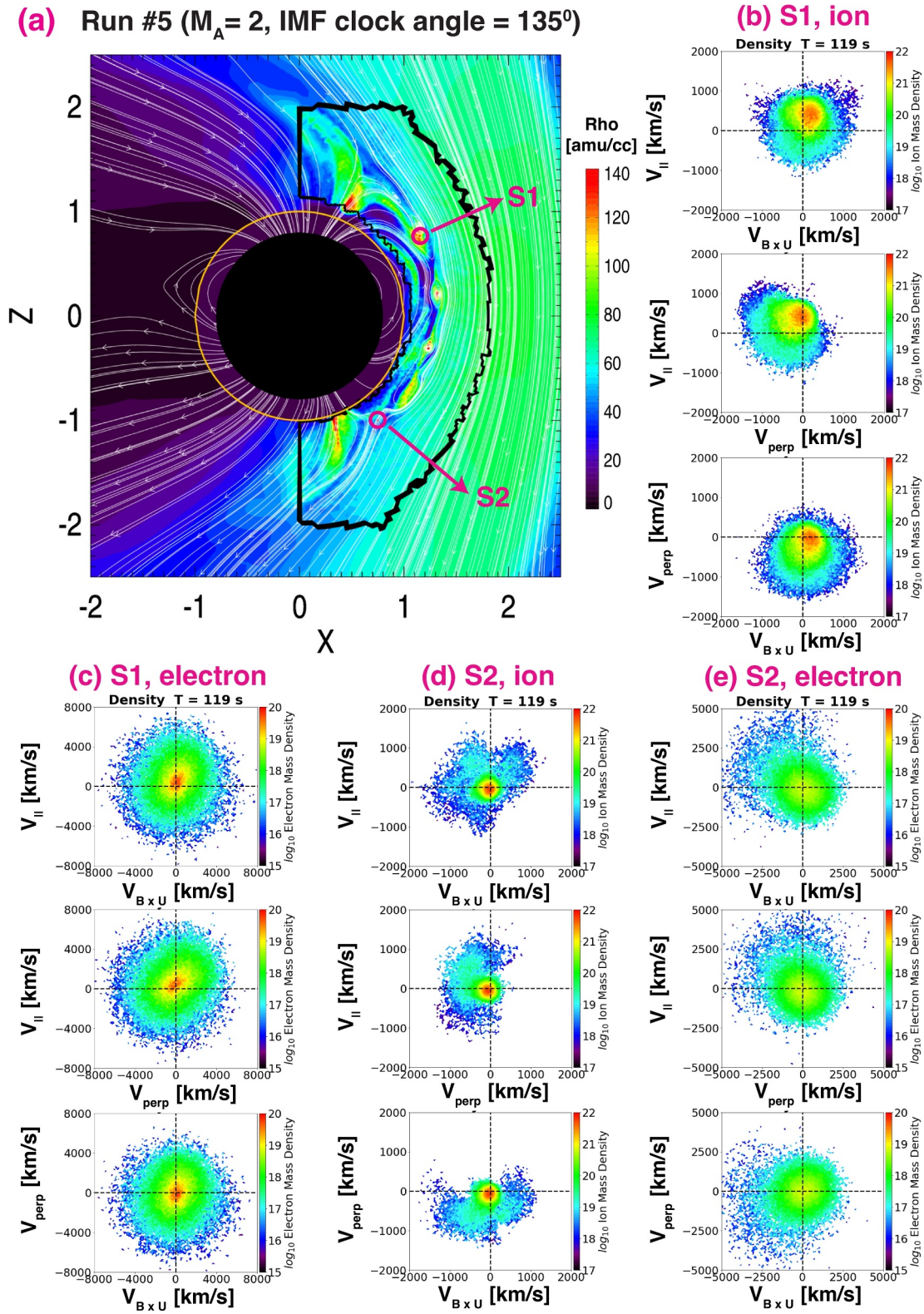

Figure 4.

3.2. Method for Identifying Reconnection X-Lines

While the examples presented in the previous sections are extracted from 2D planes to illustrate kinetic signatures associated with reconnection, magnetopause reconnection occurs over a wide range of locations in the 3D space around the magnetopause. To obtain a global picture of Mercury's magnetopause reconnection, we have developed a novel metric and algorithm to facilitate automated identification of reconnection X-lines in the MHD-AEPIC simulation. Previous studies have employed various metrics to identify reconnection sites and electron diffusion regions (EDRs). Some examples of those metrics are: (a) $\boldsymbol{E} + \boldsymbol{V} \times \boldsymbol{B}$, which quantifies the degree of violation of the frozen-in condition, (b) Nongyrotropy measures that assess particle distribution function's deviation from circular symmetry around the magnetic field direction, and (c) Local energy dissipation rate. We have conducted extensive tests on our simulations using multiple metrics and evaluated their correlation with reconnection X-lines identified based on magnetic topology. Among these metrics, we have found four quantities that demonstrate robust capabilities in helping to locate the reconnection sites in Mercury's magnetopause environment. They are: (a) Lorentz reconnection indicator: $\boldsymbol{L} = \boldsymbol{log_{10}}\left(\boldsymbol{c}\,\frac{|\boldsymbol{E}\times\boldsymbol{B}|}{\boldsymbol{E}^2}\right)$ (Lapenta, 2021), (b) Electron dissipation measure: $\boldsymbol{D_e} = \boldsymbol{J'}\cdot\boldsymbol{E'} = \boldsymbol{J}\cdot(\boldsymbol{E} + \boldsymbol{V_e}\times\boldsymbol{B}) - (\boldsymbol{n_i} - \boldsymbol{n_e})\boldsymbol{V_e}\cdot\boldsymbol{E}$ (Zenitani et al., 2011), (c) Nongyrotropy measure: $\boldsymbol{A\varnothing}$ (Scudder & Daughton, 2008), and (d) Another nongyrotropy measure: $\boldsymbol{Q}$ (Swisdak, 2016). The frame-independent definitions of $\boldsymbol{A\varnothing}$ and $\boldsymbol{Q}$ are given in Appendix A. The Lorentz reconnection indicator $\boldsymbol{L}$ has been found to decrease significantly near the reconnection site, where the in-plane component of the magnetic field is much reduced (Lapenta, 2021). Both $\boldsymbol{A\varnothing}$ and $\sqrt{\boldsymbol{Q}}$ represent the nongyrotropy of the electron pressure tensor in the plane perpendicular to the magnetic field, and they were previously observed to peak near the EDR in Ganymede's MHD-EPIC simulations (Zhou et al., 2020).

All the parameters involved in calculating the various quantities described above can be obtained directly from the output of the PIC code in our simulation. As an example, Figure 5 shows a snapshot of the various quantities in the noon-midnight meridional cut taken from Run #1 ($M_A = 6$, IMF clock angle = 180°). Note that the background colors are only plotted within the active PIC region. Figures 5a–5c show the ion density, out-of-plane magnetic field component or equivalently the core field (B_y), and ion scalar pressure (P), respectively. Notably, at this particular timestamp, three FTE-type flux ropes, separated by multiple reconnection X-lines, are present on the magnetopause. Each of these flux ropes exhibits notable enhancements in ion density, B_y and thermal pressure. The subsequent panels, Figures 5d–5g, show the four reconnection metrics $\boldsymbol{L}$, $\boldsymbol{D_e}$, $\boldsymbol{A\varnothing}$, and $\sqrt{\boldsymbol{Q}}$, respectively. We note that panel (d) employs a reversed rainbow colormap, with the minimum and maximum values represented by red and blue colors, respectively. The first reconnection metric, $\boldsymbol{L}$, exhibits a notable decrease near the EDR and within the cross-section area of the FTE located in the southern hemisphere. The second reconnection metric, $\boldsymbol{D_e}$, peaks near the reconnection X-lines but also shows elevated values inside all three FTEs. The third reconnection metric, $\boldsymbol{A\varnothing}$, demonstrates the best performance at this selected timestamp, with its value increasing significantly at three reconnection sites ($Z \sim 0.7\ R_M$, $-0.1\ R_M$, $-0.7\ R_M$) on the magnetopause surface compared to neighboring regions. Lastly, the final reconnection metric, $\sqrt{\boldsymbol{Q}}$, behaves similarly to $\boldsymbol{A\varnothing}$ in that it peaks around the three X-lines. However, it also shows enhanced values at the outer edge of the FTE near the northern cusp.

We have examined the aforementioned reconnection metrics for all the six simulations (Runs #1–6), and found that the effectiveness of individual reconnection metrics in identifying reconnection X-lines varies over different timesteps. Such variability, which was previously reported in Zhou et al. (2020), can be attributed to the complex nature of the kinetic reconnection processes. For example, Shay et al. (2016) also found that the violation of the frozen-in condition and nongyrotropic distributions themselves do not uniquely define the EDR at the X-line and suggested that complementary approach is required for more precise identification. To address the issue pertaining to varying performance of reconnection metrics ($\boldsymbol{L}$, $\boldsymbol{D_e}$, $\boldsymbol{A\varnothing}$, and $\sqrt{\boldsymbol{Q}}$) over different timesteps, we have designed a synthesized reconnection score $\boldsymbol{S}$ in this paper to consistently identify the X-lines in our MHD-AEPIC simulation. The synthesized reconnection score $\boldsymbol{S}$ is defined as follows and evaluated at each timestep.

Figure 4. Phase-space distributions for ions and electrons extracted from Run #5 ($M_A = 2$, interplanetary magnetic field clock angle = 135°) at $T = 119$ s. Panel (a) shows the global configuration of the simulated magnetosphere in the XZ plane. The red circles mark the locations of two virtual satellites placed in the simulation to sample distribution functions. Virtual satellite S1, at $X = 1.15\ R_M$, $Y = 0\ R_M$, $Z = 0.77\ R_M$, is located within an flux transfer event and satellite S2, at $X = 0.75\ R_M$, $Y = 0\ R_M$, $Z = -1.0\ R_M$, lies in the southern cusp. Panels (b) and (c) show the ion and electron distributions extracted at S1, respectively, whereas panels (d) and (e) show the distributions extracted at S2.

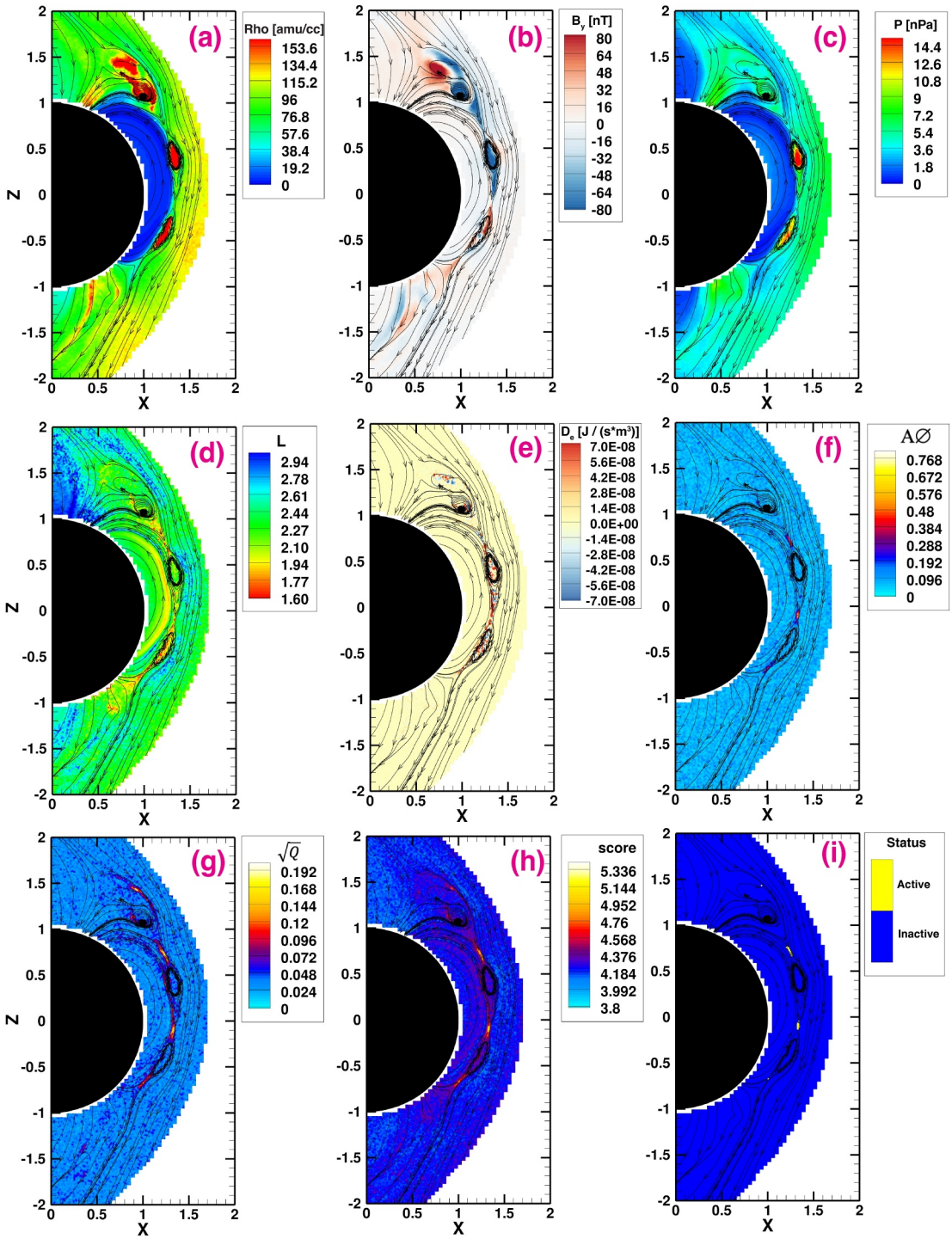

Figure 5. Snapshot of various quantities relevant to reconnection in the meridional cut ($Y = 0$) through the PIC domain taken from Run #1 ($M_A = 6$, interplanetary magnetic field clock angle = 180°) at $T = 102$ s. Mercury is represented by the solid black disk. Sampled magnetic field lines are overplotted as black arrowed lines to delineate the magnetospheric configuration. The background colors in different panels are (a) Ion density, (b) B_y, (c) Ion pressure P, (d) Lorentz reconnection indicator L, (e) Electron dissipation measure D_e, (f) and (g) Nongyrotropy measures $A\varnothing$ and $\sqrt{Q}$, (h) Synthesized reconnection score S, (i) Status of active reconnection obtained by filtering the synthesized score.

$$\boldsymbol{S} = 10^{\frac{1}{4}*\frac{3-\boldsymbol{L}}{3-\min(\boldsymbol{L})}} + 10^{\frac{1}{4}*\frac{\boldsymbol{D_e}}{\max(\boldsymbol{D_e})}} + 10^{\frac{1}{4}*\frac{\boldsymbol{A\varnothing}}{\max(\boldsymbol{A\varnothing})}} + 10^{\frac{1}{4}*\frac{\sqrt{\boldsymbol{Q}}}{\max(\sqrt{\boldsymbol{Q}})}} \quad (2)$$

where $\min(\boldsymbol{L})$ is the minimum value of $\boldsymbol{L}$ inside the active PIC region for a given timestep, and $\max(\boldsymbol{D_e})$, $\max(\boldsymbol{A\varnothing})$, $\max(\sqrt{\boldsymbol{Q}})$ are the maximum values of $\boldsymbol{D_e}$, $\boldsymbol{A\varnothing}$, and $\sqrt{\boldsymbol{Q}}$, respectively. Instead of averaging the normalized reconnection metrics linearly, each term on the righthand side (RHS) of Equation 2 is amplified exponentially to increase the separation between regions with and without active reconnection. The theoretical lower bound and upper bound of $\boldsymbol{S}$ are 2 and $4 \times 10^{1/4}$ (~7.11), respectively. Based on the definition in Equation 2, it is expected that $\boldsymbol{S}$ peaks near the X-lines and EDRs. We also note that our design of $\boldsymbol{S}$ is flexible and can be easily extended to include more reconnection metrics by adjusting their weights (constant coefficient of exponent in each term on the RHS of Equation 2) correspondingly. Figure 5h shows the values of $\boldsymbol{S}$ in the $Y = 0$ plane at $T = 102$ s from Run #1. The calculated reconnection score exhibits prominent enhancements in the close vicinities of the three X-lines ($Z \sim 0.7$ R_M, -0.1 R_M, -0.7 R_M) on the magnetopause and remains relatively small within the FTEs. Such behaviors of $\boldsymbol{S}$ are consistent with our expectations. We also observe that $\boldsymbol{S}$ increases at the edges of the FTE near the northern cusp, which is due to the enhancement of $\sqrt{\boldsymbol{Q}}$ in the same regions.

To determine whether reconnection is present at a given location, we have set an ad hoc threshold of 4.9 to filter the synthesized reconnection score, $\boldsymbol{S}$, and the outcome is shown in Figure 5i. The yellow colors ($\boldsymbol{S} > 4.9$) indicate that reconnection is active (or present) at that location, while the blue colors ($\boldsymbol{S} < 4.9$) indicate absence of reconnection. We have tested 7 different thresholds from 4.7 to 5.0 with a step size of 0.05 and determined that 4.9 works reasonably well for all of our simulations in that this threshold is able to capture the vast majority of X-lines and, at the same time, is conservative enough to filter out most of the false positives, making it a judicious choice for the purpose of our analysis. As shown in Figure 5i, the X-lines at $Z \sim 0.7$ R_M and -0.1 R_M are clearly marked by two yellow stripes, the other X-line at $Z \sim -0.7$ R_M is marginally discernible by a small area of yellow coloring due to our conservative choice of the threshold. These results suggest that our approach, which involves the calculation of synthesized reconnection score $\boldsymbol{S}$ followed by a filtering process, is highly effective in identifying the precise locations of X-lines in the meridional cut of the active PIC region.

The performance of our reconnection X-line identification algorithm has also been validated for the 3D PIC domain. Figure 6 shows a series of snapshots of ion density isosurfaces (orange surfaces corresponding to $\rho_i = 180$ amu/cc) and reconnection score isosurfaces (red surfaces corresponding to score $\boldsymbol{S} = 4.9$) in 3D taken at different timesteps from Run #1. Since the red surfaces are defined as $\boldsymbol{S} = 4.9$, they effectively indicate the identified X-lines in 3D geometry. Mercury is represented by the gray sphere in the center. Ion density contours in the $Y = 0$ and $Z = 0$ planes are also given in Figure 6 to provide global context. As indicated by the sampled magnetic field lines (black arrowed lines), the enhanced density regions are located mostly within the flux ropes, suggesting that FTEs carry a dense population of plasmas while moving along the magnetopause surface. In Figure 6a, there are two FTEs: one large FTE (labeled as F1) located near the equatorial plane and another small FTE (labeled as F2) located in the northern dusk sector of the magnetopause. Each of the two FTEs is accompanied by two X-lines situated to its north and south. Twelve seconds later, as shown in Figure 6b, F2 has evolved into a medium-size FTE with well-developed twisted magnetic field lines enveloping the corresponding ion density isosurface. In Figure 6c, two smaller FTEs have formed in addition to the primary FTE F1 seen in Figure 6a: one in the southern dawn sector (labeled as F3) and another in the northern dusk sector (labeled as F4). Both FTEs are observed to locate between two identified reconnection X-lines, indicating that the FTEs were generated by multiple X-line reconnection in the simulation. The presence of such geometry, which is characterized by FTEs surrounded by two adjacent X-lines, is also clearly reflected in Figures 6d–6f, suggesting that our set of selection criteria for X-lines not only have reliable performance for the 2D meridional plane but also are robust in capturing reconnection sites in 3D.

The varying intensity of reconnection can also be captured appropriately by applying our automated identification algorithm. As depicted in Figure 6e, there are three FTEs observed in close proximity to the equatorial plane. In particular, the first FTE is positioned in the dawn sector (labeled as F5), the second FTE traverses the meridional plane (labeled as F8), and the third FTE resides within the dusk sector (labeled as F9). Seven seconds later (Figure 6f), F5 has moved in both the $-Y$ and $-Z$ directions from its previous position, while F8 and F9 remain situated near the equatorial plane. However, all three FTEs undergo significant changes in their sizes as they interact with the surrounding plasma and magnetic field. Specifically, FTE F5 exhibits a reduction in its cross-

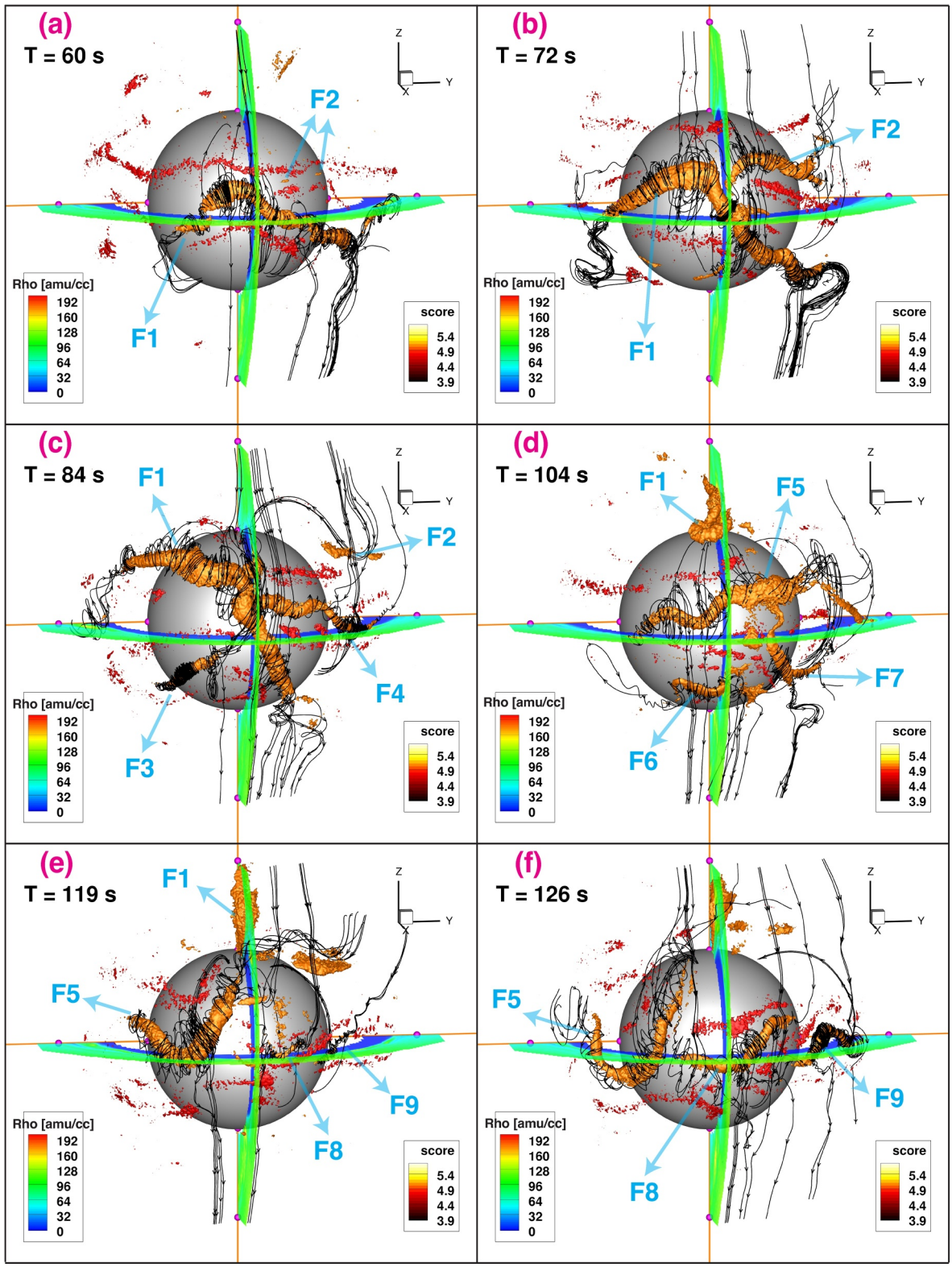

Figure 6.

section area while preserving its length in the *Y* direction, and the signature of identified X-lines surrounding F5 becomes weaker from Figures 6e and 6f. In contrast, both FTEs F8 and F9 have expanded in the axial direction (which is roughly aligned with the *Y*-axis for 180° clock angle IMF) and cross-sectional direction, and their corresponding adjacent X-lines display significant broadening in both *Y*- and *Z*-direction. These observations indicate that, in our simulations, The growth and decay of FTEs are typically associated with enhanced and reduced reconnection intensity, respectively, which is consistent with previous observations from Magnetospheric MultiScale (MMS) mission (Akhavan-Tafti, Slavin, Eastwood, et al., 2019) and the general expectation that the plasmas carried by FTEs are supplied primarily by reconnection outflows (Akhavan-Tafti, Slavin, Sun, et al., 2019).

3.3. Dawn-Dusk Asymmetries in Magnetopause Reconnection Occurrence and Electric Field

The spatial distribution of reconnection occurrence in Mercury's tail plasma sheet has been investigated extensively in prior works. Previous studies from MESSENGER observations (Sun et al., 2016) have demonstrated the presence of a dawn-dusk asymmetry in tail reconnection occurrence. Specifically, it has been shown that the reconnection events tend to happen preferentially in the dawn sector (or the post-midnight region) of the tail. With our MHD-AEPIC simulations that used an active PIC region to cover the dayside magnetopause, our analysis in this study will, instead, focus on investigating the distribution of reconnection occurrence at the dayside magnetopause. To quantify the distribution of reconnection occurrence, we have made a 2D rectangular graph for each simulation showing the aggregated reconnection probability in Magnetic Local Time (MLT) and geographic latitude coordinates and the results for all six simulations are summarized in Figure 7.

The method we used to calculate aggregated reconnection probability is outlined as follows: First, we compute the synthesized reconnection score $\boldsymbol{S}$ within the 3D active PIC domain for every timestep for which the simulation results were saved (i.e., every 1 s). Second, we count the number of times where a given grid point exhibits a value of $\boldsymbol{S}$ exceeding the designated threshold of 4.9 across all timesteps. These aggregated counts are subsequently linked to their corresponding grid points. Each grid point is then projected onto the two-dimensional MLT and latitude coordinates depicted in Figure 7. Lastly, we partition the two-dimensional MLT-latitude coordinates into discrete bins (or boxes), each measuring 0.1 h of MLT × 3° of latitude in size. The aggregated reconnection probability is then calculated by dividing the value within each box by the total sum of values across all boxes.

Comparing all the panels in Figure 7 indicates that there is a close correlation between the primary locations of reconnection X-lines on the magnetopause and the IMF clock angle in the upstream solar wind. For instance, the locations of X-lines in the 180° clock angle IMF cases (top row) are primarily concentrated in a horizontal band centered around Mercury's magnetic equator, which is slightly above the geographic equator due to Mercury's offset dipole. When the IMF clock angle is 135° or 90°, the primary X-line locations are tilted with respect to the equatorial plane. The tilt angle is roughly 22.5° for the 135° IMF cases (middle row) and 45° for the 90° IMF cases (bottom row). Such correlation is consistent with the expectation that reconnection tends to occur at places of maximum magnetic shear, that is, where the magnetic fields in the magnetosphere and magnetosheath are anti-parallel to each other.

The results shown in Figure 7 further reveal some intriguing dawn-dusk asymmetries in the reconnection occurrence predicted by our MHD-AEPIC simulation. In all six cases, the distribution of reconnection probability exhibits a more diffusive pattern on the dawnside, characterized by a larger area in which reconnection can potentially occur. To assess the distribution of identified reconnection events in a more quantitative manner, we have calculated the probabilities of reconnection (P) occurring on the dawn side (MLT < 12) and on the dusk side (MLT > 12). The results are shown as white texts inside each panel in Figure 7. Across all six cases, the probability of reconnection occurring on the dawn side ranges from 56% to 72%, indicating a notable dawn-dusk asymmetry. For simulations with the same IMF orientations, the dawn-dusk asymmetry becomes more prominent

Figure 6. 3D geometry of flux transfer events (FTEs) and reconnection sites identified in the simulation as shown by multiple snapshots of ion density isosurfaces (orange surfaces corresponding to $\rho_i = 180$ amu/cc) and synthesized reconnection score isosurfaces (red surfaces corresponding to $\boldsymbol{S} = 4.9$). The results were extracted from Run #1 ($M_A = 6$, interplanetary magnetic field clock angle = 180°). Sampled magnetic field lines are plotted as the black arrowed lines to show the geometry of the magnetic field. Color contours of ion density in both $Y = 0$ and $Z = 0$ cuts of the PIC region are overplotted to illustrate the spatial orientation and location. Labels and arrows are added to denote FTEs. Mercury is represented by the gray sphere in the center. The distance between neighboring magenta balls along the axes in each panel is 1 R_M.

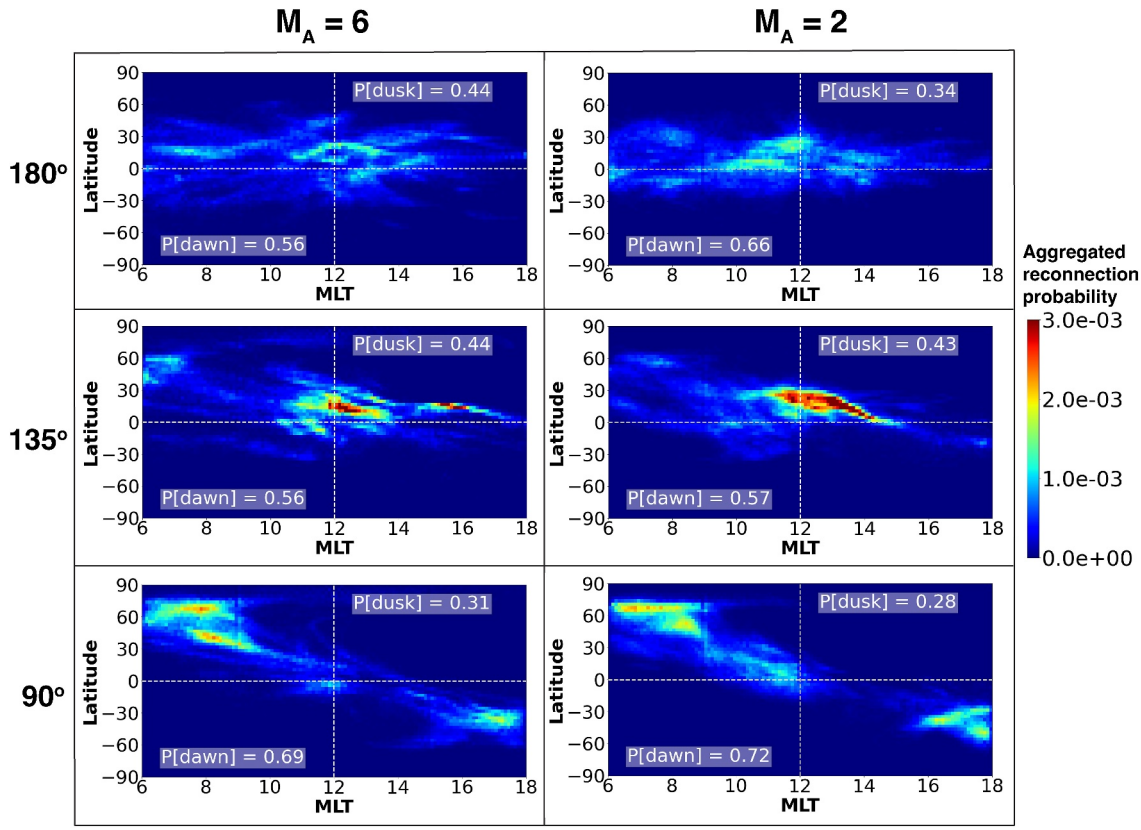

Figure 7. Aggregated dayside reconnection probability shown in 2D MLT-latitude coordinates for all six simulations. The method used for calculating the aggregated reconnection probability is described in detail in Section 3.3. The legends located in the bottom-left and top-right corners of each panel display the probabilities of reconnection occurring on the dawnside (MLT < 12) and duskside (MLT > 12), respectively.

for solar wind $M_A = 2$ compared to $M_A = 6$, possibly due to the increased strength of the IMF set in the simulation. We will return to this point later in the Discussion section. For simulations with identical M_A numbers, the 90° IMF cases exhibit the strongest dawn-dusk asymmetry when compared to the 180° and 135° cases, with approximately 70% of reconnection events occurring on the dawn side. In all six cases, magnetopause reconnection appears to show a consistent preference for occurring on the dawn side. Such a dawn-dusk asymmetry, as predicted by our MHD-AEPIC simulations, would suggest that the upstream solar wind plasma may enter Mercury's magnetosphere via reconnection preferentially on the dawn side, and the resultant energetic particle precipitation into Mercury's cusps is then expected to also exhibit preference toward dawn. Possible explanations for such dawn-dusk asymmetry in reconnection occurrence will be discussed in the Discussion section.

Given that non-ideal electric fields play a central role in magnetic reconnection, where it facilitates the conversion of magnetic energy to particle energy (Schindler et al., 1988), we have conducted further analysis to investigate the spatial distributions of the non-ideal electric field simulated by the MHD-AEPIC model. Specifically, we examine the parallel component of the electric field in the electron's co-moving frame $\boldsymbol{E}_{\text{non-ideal}}$, defined as follows, as a proxy for the non-ideal electric field.

$$\boldsymbol{E}_{\text{non-ideal}} = (\boldsymbol{E} + \boldsymbol{V}_e \times \boldsymbol{B}) \cdot \frac{\boldsymbol{B}}{|\boldsymbol{B}|} \tag{3}$$

where $\boldsymbol{E}$ represents the electric field, $\boldsymbol{V}_e$ denotes the electron bulk velocity, and $\boldsymbol{B}$ represents the magnetic field. For this analysis, we have calculated $\boldsymbol{E}_{\text{non-ideal}}$ on the magnetopause surface for each timestep. The magnetopause surface in the simulation was determined based on the Shue et al. (1997) empirical model (which was shown to work reasonably well for Mercury by Winslow et al. (2013)), with dynamically adjusted parameters involved in

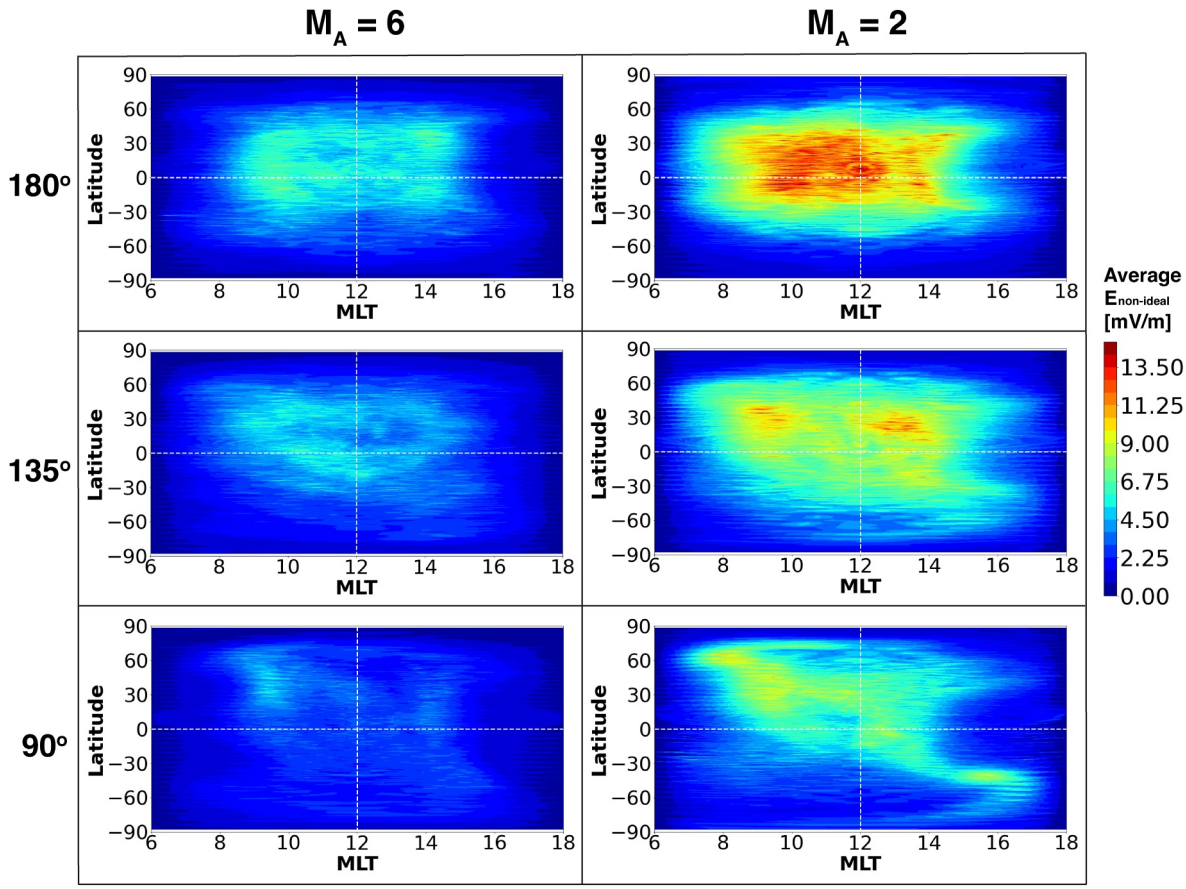

Figure 8. Time-averaged non-ideal electric field $E_{\text{non-ideal}}$ shown in 2D MLT-latitude coordinates for all six simulations. $E_{\text{non-ideal}}$ is defined as the parallel component of the electric field in the electron's co-moving frame.

the empirical model at each timestep to account for the temporarily varying shape and location of the simulated magnetopause, following the same approach as described in Li et al. (2023). Figure 8 presents the distributions of time-averaged $\boldsymbol{E}_{\text{non-ideal}}$ for all six simulations, following the same format as Figure 7. The MLT-latitude graphs shown in Figure 8 clearly demonstrate that the non-ideal electric field exhibits systematic variations in both its strength and spatial distribution in response to changes in the upstream solar wind conditions. Specifically, $\boldsymbol{E}_{\text{non-ideal}}$ shows a trend of increasing magnitude with decreasing solar wind M_A and increasing IMF clock angle, consistent with the expected influence of these two parameters on the reconnection intensity as they primarily control the magnetosheath plasma β and the magnetic shear across the magnetopause boundary. The spatial distribution of $\boldsymbol{E}_{\text{non-ideal}}$ exhibits a similar pattern as that of the corresponding primary X-line, as observed in Figure 7. Such a behavior is consistent with the expectation that the non-ideal electric field tends to peak in close proximity to the primary X-line. In addition, the spatial distribution of $\boldsymbol{E}_{\text{non-ideal}}$ displays a noticeable dawn-dusk asymmetry similar to that observed in the aggregated reconnection score distribution. In all six simulations, there is a clear shift in the center of the $\boldsymbol{E}_{\text{non-ideal}}$ distribution toward the dawn side of the magnetopause. Moreover, the magnitude of this shift is found to correlate with the probability of reconnection occurring on the dawn side (P [dawn] shown in Figure 7). The asymmetric spatial distributions of $\boldsymbol{E}_{\text{non-ideal}}$ and reconnection probability suggest that there is an inherent dawn-dusk asymmetry in reconnection occurrence in our simulations. We will further discuss this point in the Discussion section by suggesting possible mechanisms that may account for such an asymmetry.

3.4. Statistical Properties of FTEs as Simulated by PIC

As seen in the examples shown in previous sections, FTEs with rope-like magnetic topology are formed frequently in our MHD-AEPIC simulation. They arise as a result of multiple X-line reconnection and carry solar

wind plasma and open magnetic flux into the magnetosphere, which eventually participate in the global circulation of plasma and magnetic flux, or the so-called "Dungey-cycle." It is, therefore, of interest to characterize the properties of FTEs and quantitively assess their contribution to the global convection and dependence on the upstream conditions based on our simulation results. The properties of FTEs we focus on here are their temporal spacing (or equivalently, recurrence rate), spatial size, traveling speed, core field strength, plasma density, magnetic flux content, and overall contribution to open flux generation in the magnetosphere. In our statistical analysis presented below, we have utilized the maximum values of plasma density and core field strength across the cross-section of an FTE to represent its characteristic density and core field strength, acknowledging that their distributions within the FTE typically are non-uniform. The meanings of other properties are as follows: temporal spacing refers to the time interval between the centers of neighboring FTEs; traveling speed denotes the average speed at which an FTE traverses along the magnetopause surface; FTE size is characterized by its length in the latitudinal direction multiplied by a geometric factor $\cos(\theta_{\mathrm{FTE}})$, where θ_{FTE} is the angle between the horizontal direction and the FTE axis. For further details regarding the techniques employed to extract the characteristics of FTEs, we refer the readers to our previous work on FTEs based on global Hall-MHD simulations (Li et al., 2023).

Figures 9–11 present histograms of FTE size, traveling speed, core field strength, and magnetic flux content extracted from our MHD-AEPIC simulations for different solar wind and IMF conditions. To facilitate effective comparison, simulations with the same IMF clock angles but different solar wind M_A are grouped into a single figure (Figure 9 for 180° IMF clock angle, Figure 10 for 135° clock angle, and Figure 11 for 90° clock angle). We have taken the average of FTE size over its entire evolution to obtain the mean FTE size, which is shown in panels (a) and (e) in Figures 9–11. Across all simulations, the FTE size ranges from ∼300 to ∼2,700 km and the breadth of the size distribution exceeds 1,000 km, suggesting that even under constant upstream conditions, FTEs formed on Mercury's magnetopause can exhibit considerable variability in their spatial sizes. For the three IMF clock angles investigated in this paper, the average FTE size (shown in the legends of panels (a) and (e)) is found to increase monotonically with decreasing IMF clock angle, but appear to be less sensitive to changes in the solar wind M_A, that is, the average size is comparable between different M_A numbers for the same IMF clock angle.

The distributions of FTE traveling speed are shown in panels (b) and (f) of Figures 9–11, with the positive and negative values corresponding to northward and southward propagation, respectively. The traveling speeds of FTEs fall into a range spanning from −500 km/s to 600 km/s. For all IMF clock angles, the average traveling speeds follow an upward trend as the solar wind M_A decreases. Additionally, there is a roughly even distribution of FTEs traveling in the northward and southward directions, except for the 90° clock angle simulations where FTEs appear to favor southward propagation. This deviation from the general trend may be attributed to the presence of dawn-dusk asymmetry in reconnection probability, which has been presented in Section 3.3. This asymmetry results in higher occurrence of multiple X-line reconnections in the dawn sector, which consequently leads to an increased number of FTEs originating in the dawn sector, specifically to the south of the primary reconnection X-line (the geometry of which has been shown in Section 3.3). These FTEs inherit the dominant southward motion driven by the reconnection outflow upon formation, thereby resulting in a preference for southward propagation.

Panels (c) and (g) in Figures 9–11 show the distributions of FTE core field strength for all simulations. The mean core field strength falls within the range of 66–212 nT, which is consistent with the findings reported by Sun et al. (2020) for FTE shower events observed by MESSENGER. The polarity of the FTE core field indicates its alignment with respect to the dawn-dusk direction (Y-axis). In simulations with an IMF clock angle of 180°, both positive and negative core fields are present for the FTEs formed in the simulation with an approximately even distribution. In contrast, in the presence of a significant B_y component in the upstream IMF (i.e., 135° and 90° clock angle simulations), almost all FTEs exhibit a negative polarity in their core fields, which is the same direction as the ambient IMF B_y imposed in the simulation. This dependence of FTE core field polarity on the upstream B_y component of the IMF is consistent with previous findings from our Hall MHD simulations (Li et al., 2023) and observations of FTEs at the Earth's magnetopause by the MMS mission (Kieokaew et al., 2021). Both our simulation results and in situ observations suggest that the orientation of the reconnection guide field, which largely depends on the upstream IMF in the case of Mercury (and Earth), plays a crucial role in establishing the polarity of the FTE core field. Furthermore, the average core field strength of FTEs increases with decreasing solar wind M_A and with decreasing IMF clock angle. These findings are entirely consistent with the observed dependence of FTE core field strength reported by Sun et al. (2020).

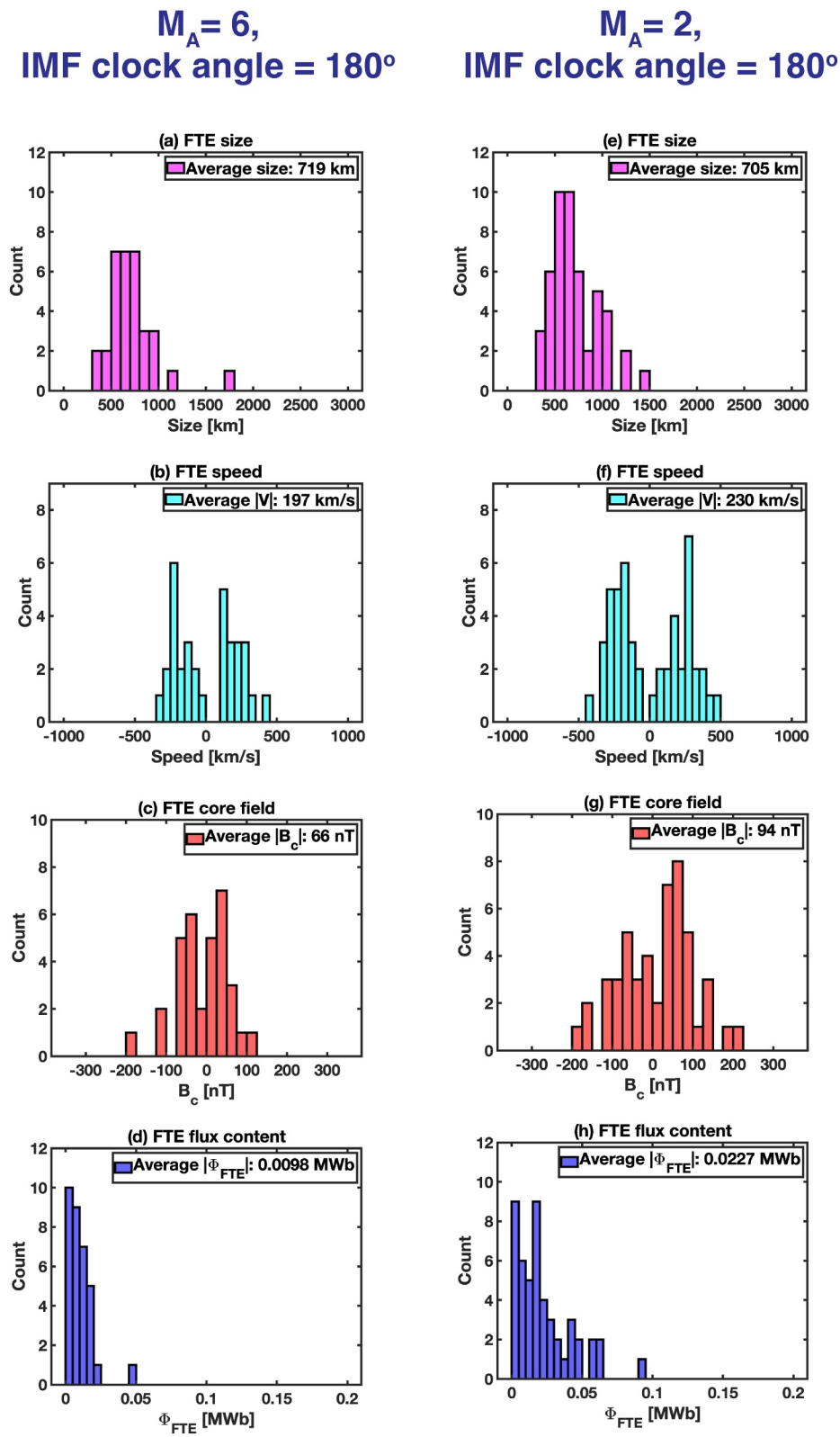

Figure 9. Histograms of flux transfer event (FTE) properties for the 180° interplanetary magnetic field clock angle cases with different solar wind M_A. (a) and (e) Average FTE size. (b) and (f) Average FTE speed along the direction perpendicular to its axis. (c) and (g) Core field strength. (d) and (h) Magnetic flux carried by FTE. The left column corresponds to $M_A = 6$ and the right column is for $M_A = 2$.

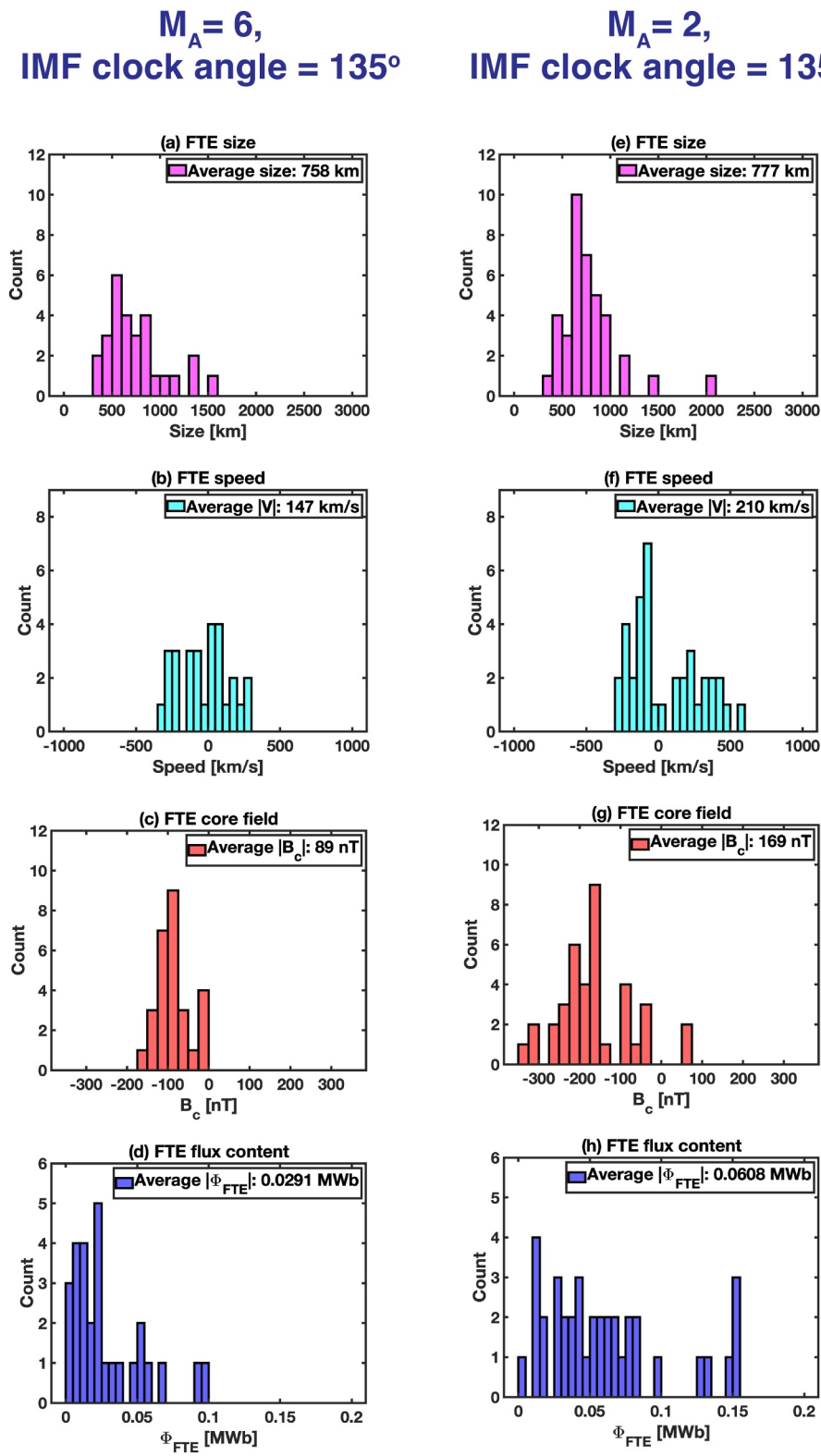

Figure 10. Same as Figure 9, but for 135° interplanetary magnetic field clock angle cases.

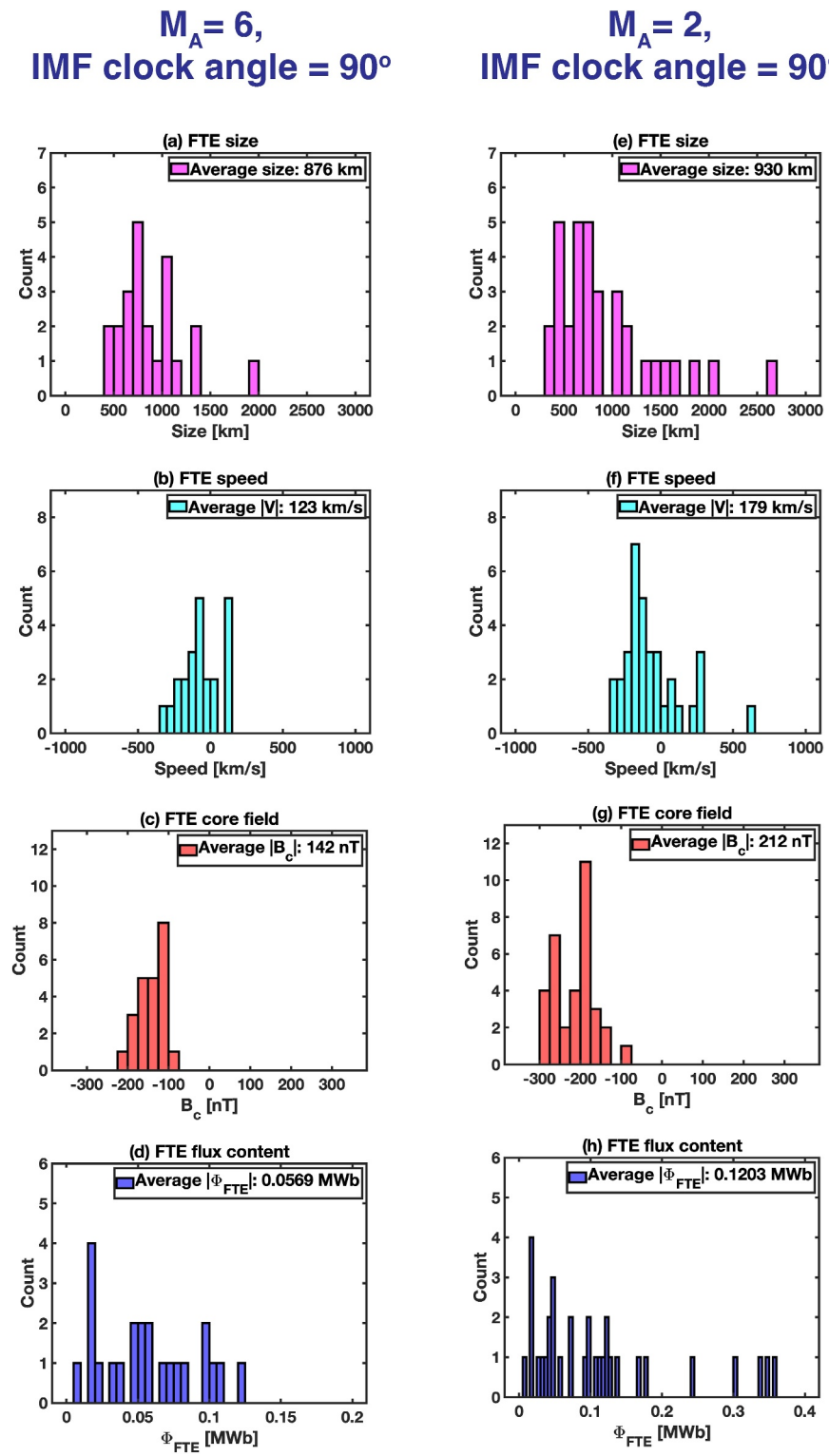

Figure 11. Same as Figure 9, but for 90° interplanetary magnetic field clock angle cases.

The distributions of magnetic flux content carried by FTEs (in the form of flux ropes) are shown in panels (d) and (h) of Figures 9–11. The average open flux carried by FTEs under different solar wind and IMD conditions ranges from 0.01 to 0.12 MWb. The maximum amount of open flux carried by FTEs seen in our simulations is

Table 2
Comparison of Simulated Flux Transfer Event Properties, Polar Cap Open Flux, and Cross Polar Cap Potential for Different Solar Wind M_A and Interplanetary Magnetic Field Clock Angles

	Upstream conditions					
	$M_A = 6$			$M_A = 2$		
FTE properties	Clock angle 180° (Run #1)	Clock angle 135° (Run #2)	Clock angle 90° (Run #3)	Clock angle 180° (Run #4)	Clock angle 135° (Run #5)	Clock angle 90° (Run #6)
Simulation duration	200 s	200 s	200 s	200 s	200 s	200 s
Total number of FTEs	33	28	23	49	38	34
Average recurrence rate (or temporal spacing)	1 FTE every 6.1 s	1 FTE every 7.5 s	1 FTE every 8.7 s	1 FTE every 4.1 s	1 FTE every 5.3 s	1 FTE every 5.9 s
Average density	139 amu/cc	111 amu/cc	93 amu/cc	132 amu/cc	102 amu/cc	77 amu/cc
Average size	719 km	758 km	876 km	705 km	777 km	930 km
Average speed	197 km/s	147 km/s	123 km/s	230 km/s	210 km/s	179 km/s
Average core field	66 nT	89 nT	142 nT	94 nT	169 nT	208 nT
Average flux content	0.010 MWb	0.029 MWb	0.057 MWb	0.023 MWb	0.061 MWb	0.120 MWb
Average polar cap open flux content	3.51 MWb	3.45 MWb	2.65 MWb	4.38 MWb	3.95 MWb	3.02 MWb
Cross Polar Cap Potential	56 kV	50 kV	25 kV	130 kV	101 kV	56 kV
FTE contribution to open flux circulation	2.9%	8.1%	26.2%	4.3%	11.5%	36.4%

~0.36 MWb (see Figure 11h), which is very close to the upper limit of ~0.4 MWb reported from MESSENGER observations (Sun, Dewey, et al., 2022). Imber et al. (2014) conducted a survey of MESSENGER magnetic field data and identified 17 "large" FTEs. By modeling the FTEs as force-free flux ropes, they estimated the average flux content of these 17 "large" FTEs to be 0.06 MWb, which closely aligns with our simulation results, especially those for Run #3 and #5. However, the higher end of simulated average FTE flux content (seen in Run #6) is about twice the estimate by Imber et al., suggesting that our $M_A = 2$, 90° IMF clock angle simulation may represent a scenario of stronger solar wind driving than considered by the Imber et al. study. Our simulation results also show that when considering the same IMF clock angle, individual FTEs transport approximately twice the amount of open flux for solar wind $M_A = 2$ compared to $M_A = 6$. For both $M_A = 6$ and $M_A = 2$ simulations, the average magnetic flux carried by FTEs follows a consistent, increasing trend as the IMF clock angle decreases, which is in good agreement with the trend found in the statistical study of MESSENGER FTE shower events by Sun et al. (2020).

To summarize the results, we compare in Table 2 key statistics pertaining to simulated FTEs as well as the total open flux content in the polar cap and the cross polar cap potential (CPCP) for all six simulations. The latter two quantities (i.e., total open flux and CPCP) provide a global measure of the solar wind-magnetosphere coupling, which can be used as context to evaluate the contributions of FTEs in driving the global convection and dynamics. The methodology used to calculate CPCP is described in detail in Zhou et al. (2020), which has also been successfully applied to our previous Hall-MHD simulations of Mercury's magnetosphere (Li et al., 2023). As can be seen from Table 2, the temporal separation between adjacent FTEs spans from 4.1 to 8.7 s. Comparing the results among simulations using different upstream conditions reveals the following trends regarding the temporal spacing: (a) For the same IMF orientation, the spacing is smaller in simulations with solar wind $M_A = 2$ compared to those with $M_A = 6$. (b) The spacing decreases with increasing IMF clock angle in simulations with the same solar wind M_A. Both the range and trend of the FTE temporal spacing derived from our simulations exhibit good agreement with the MESSENGER observations during FTE shower events (Sun et al., 2020). These results together suggest that FTEs at Mercury tend to occur more frequently when the upstream solar wind driving is more favorable for reconnection onset, that is, low M_A solar wind and large shear angle IMF.

As indicated in Table 2, the time-average of the peak plasma density within FTEs varies between 77 and 139 amu/cm^3. In both $M_A = 6$ and $M_A = 2$ simulations, the FTE density is found to decrease with decreasing IMF clock angle. For all three IMF clock angles investigated in this study, the characteristic FTE density is found to decrease

with decreasing solar wind M_A. The reduced plasma density under smaller solar wind M_A could be accounted for by the dependence of the properties of the magnetosheath on the solar wind conditions. That is, solar wind with lower M_A leads to a thicker magnetosheath with less dense plasma compared to higher M_A solar wind, consistent with the trend identified in MESSENGER observations (Gershman et al., 2013). The changes in the magnetosheath thickness and plasma density can be clearly observed by comparing Figure 1a with Figure 2a.

The average polar cap open flux content and average CPCP in the simulations range from 2.65 to 4.38 MWb and 25–130 kV, respectively. Both quantities increase with decreasing solar wind M_A and increasing IMF clock angle. Such a trend is consistent with the expectation that reconnection occurring at the dayside magnetopause tends to favor a low plasma β environment and an anti-parallel configuration of the magnetic field (Sun et al., 2020; Swisdak et al., 2010). By comparing the flux content associated with all FTEs with the total open flux in the polar cap, we find that, on average, approximately 0.28%–3.97% of the total open flux content within the polar cap is contributed by FTEs, which is in accordance with the previously reported range in Sun, Dewey, et al. (2022).

To further determine the role of FTEs in driving the Dungey-cycle at Mercury, we estimate FTEs' overall contribution to the open flux generation on the dayside by calculating $(\Phi_{avg} * N_{FTE})/(CPCP*T)$, where Φ_{avg} is the average open flux carried by FTEs as shown in the legends of panels (d) and (h) in Figures 9–11, N_{FTE} is the total number of identified FTEs in the simulation, T represents the duration of the simulation, which is 200 s for all six cases. The numerator $\Phi_{avg} * N_{FTE}$ denotes the total amount of magnetic flux transported by FTEs during the simulation, and the denominator $CPCP*T$ indicates the total amount of open flux generated at the dayside magnetopause, which presumably includes contributions from FTEs resulting from multiple X-line reconnection as well as single X-line reconnection that also produces open flux but not FTEs. As indicated in Table 2, about 2.9%–36.4% of the dayside open flux is generated through FTEs. These numbers are in agreement with the previous estimates based on MESSENGER observations (Imber et al., 2014; Slavin et al., 2012). For all three IMF clock angles (180°, 135°, and 90°), our results reveal that a higher percentage of open flux is generated by FTEs in simulations with $M_A = 2$ compared to $M_A = 6$. However, the contribution of FTE to the open flux generation appears to be primarily controlled by the IMF clock angle, as indicated by the exponentially increasing values shown in the bottom row of Table 2.

4. Discussion

4.1. Potential Mechanisms Causing Dawn-Dusk Asymmetries in Mercury's Magnetopause Reconnection

In Section 3.3, we have presented simulation evidence of dawn-dusk asymmetry in magnetopause reconnection occurrence and associated non-ideal electric field, both of which exhibit preference for the dawn side. Here we discuss several processes that could account for the dawn-dusk asymmetry found in our simulations. One of the prominent features of 3D dayside reconnection observed at the Earth's magnetopause is the spreading of reconnection X-line in the direction perpendicular to the plane of reconnection (e.g., Zou et al., 2018), which we think could also operate at Mercury. Previous studies (e.g., Nakamura et al., 2012; Shepherd & Cassak, 2012) have suggested that X-line spreading is mainly driven by two processes: one associated with the motion of the current carriers and another caused by the propagation of Alfvén waves along the out-of-plane (guide field) direction. Correspondingly, the speeds of X-line spreading in the directions of electron and ion out-of-plane flows are expressed as follows:

$$V_{Xe} = \max(V_{eg}, C_{Ag}) \tag{4}$$

$$V_{Xi} = \max(V_{ig}, C_{Ag}) \tag{5}$$

where V_{eg} and V_{ig} represent the out-of-plane flow speeds of electrons and ions contributing to carrying the electric currents, and C_{Ag} denotes the Alfvén speed based on the guide field, given by

$$C_{Ag} = \frac{B_g}{\sqrt{\mu_0 \rho}} \tag{6}$$

where B_g is the strength of the guide field and ρ is the plasma density near the reconnection site. We have sampled multiple reconnection sites in the six simulations and used Equations 4–6 to calculate the characteristic values of

V_{Xe} and V_{Xi} in each simulation. For electrons, their flow direction in the dayside magnetopause current sheet is toward the dawnside, and as such they tend to spread the X-line toward the dawn side. We find that the spreading speed due to electron motion, V_{Xe}, varies from 937 km/s to 1,551 km/s. It is worth noting that V_{Xe} is equivalent to V_{eg} across all six simulations, as the electron flow speed is significantly greater than the Alfvén speed C_{Ag}. In contrast, the ion flow tends to cause the X-line to spread toward the dusk side and the spreading speed, V_{Xi}, falls within the range of 81 km/s to 451 km/s. We note that V_{Xi} is primarily determined by the Alfvén speed C_{Ag}, except in cases with 180° IMF clock angle, where the guide field is almost absent. Comparing the calculated spreading speeds from our simulations indicates that at Mercury's dayside magnetopause, the dawnward spreading speed (V_{Xe}) of X-lines is significantly larger than the duskward spreading speed (V_{Xi}). Such difference in spreading speeds offers a plausible explanation for the observed dawn-dusk asymmetry in the reconnection occurrence and non-ideal electric field, as shown in Figures 7 and 8. Furthermore, our calculations show that, when the IMF clock angle is the same, the X-line spreading speed for electrons consistently exhibits larger values in $M_A = 2$ simulations compared to $M_A = 6$ simulations, which is consistent with the increased magnetopause current density and reduced magnetosheath plasma density seen in $M_A = 2$ cases. This enhanced dawnward X-line spreading speed in $M_A = 2$ simulations provides an explanation for the results presented in Section 3.3, which shows that the dawn-dusk asymmetry becomes more prominent in $M_A = 2$ simulations compared to $M_A = 6$ simulations for the same IMF orientations.

Another possible contributing process to the dawn-dusk asymmetry associated with the magnetopause reconnection seen in our simulations is the Hall effect. Previous study by Liu et al. (2019) demonstrated the presence of a suppression region near the reconnection site in their 3D PIC simulations, which arises due to the Hall effect in three-dimensional configuration. The spatial extent of this suppression region is of the order $10d_i$ (d_i is the ion inertial length), leading to an "internal" asymmetric structure of the X-line which is notable only in systems with sizes comparable to that of the suppression region. Given that the dawn-dusk width of Mercury's tail current sheet is $\sim 37d_i$ (Poh et al., 2017; Sun et al., 2016), this internal asymmetry has been invoked to explain various dawn-dusk asymmetries observed by MESSENGER in Mercury's magnetotail (Liu et al., 2019). Here we examine if the same Hall effect could also be present at Mercury's dayside magnetopause. In our MHD-AEPIC model, the proton density near the magnetopause reconnection sites is found to fall in the range of ~60 to ~90 cm^{-3}. After applying the scaling factor of 4, as described in Section 2.1, the effective ion inertial length d_i at the dayside magnetopause in our simulation is estimated to be around 100–120 km. The dayside magnetopause current sheet in our simulation extends in the Y direction over a distance of ~2 R_M, which is equivalent to ~40 d_i. Therefore, the dawn-dusk extent of the magnetopause current sheet in our simulation is comparable to the dimension of the suppression region, similar to the situation for the magnetotail current sheet. Therefore, it is reasonable to expect that the asymmetry resulting from the Hall effect in 3D may also contribute to the dawn-dusk asymmetries in Mercury's dayside magnetopause reconnection observed in our simulations.

4.2. Large FTEs and Their Contribution to Global Convection and Dynamics

In the statistical results of FTE properties presented in Section 3.4 and Figures 9–11, we find that FTEs formed in the simulation come with a range of sizes, including some that have scale lengths in the cross-section exceeding ~1,000 km, which we term as "large" FTEs. Various previous works have studied large FTEs based on MESSENGER data. For instance, Slavin, Lepping, et al. (2010) identified six FTEs encountered during MESSENGER's first two flybys of Mercury (M1 and M2) and estimated that a single large FTE may carry an axial magnetic flux content of ~0.2 MWb and contribute ~30 kV to the CPCP. Imber et al. (2014) further studied 58 large FTEs observed by MESSENGER and found that, on average, a large FTE carries ~0.06 MWb of flux content and contribute ~25 kV to CPCP, which suggests that large FTEs play an important role in driving global convection. Here we examine the properties of those large FTEs seen in our simulations and compare them with MESSENGER observations. The large FTEs of interest correspond to those appearing near the tail end of the FTE flux content distributions (panels (d) and (h) in Figures 9–11). Figure 12 shows one example of large FTE from Run #5 ($M_A = 2$, IMF clock angle = 135°). This particular FTE, as highlighted by the magenta box, is situated slightly south of the equatorial plane characterized by twisted magnetic field lines and enhanced plasma density within the FTE. Notably, the cross-section area of this FTE is significantly expanded in both the latitudinal and radial directions, resulting in a substantial compression to both the magnetospheric and magnetosheath plasmas adjacent to the magnetopause. The open flux carried by this large FTE is estimated to be $\Phi = 0.15$ MWb, which corresponds to 3.86% of the total polar cap flux content found in the simulation (3.95 MWb). The transfer of this

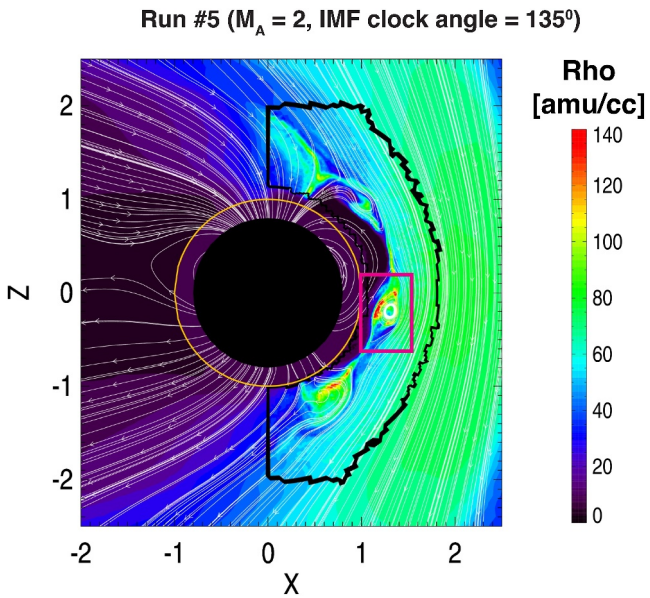

Figure 12. Snapshot of plasma density (ρ) contour in meridional plane with sample magnetic field lines overplotted as white arrowed lines. A large flux transfer event associated with density enhancements, highlighted by the magenta box, is positioned slightly south to the equatorial plane at this particular time. The data shown in this figure is extracted at T = 185 s in Run #5.

magnetic flux from the dayside to the nightside magnetosphere will contribute to the CPCP by an amount $\Phi/\Delta T$, as proposed by Slavin, Lepping, et al. (2010), where $\Delta T \equiv$ (FTE size)/(FTE speed) is the time required for the FTE's open flux to merge into the polar cap. For this FTE, the value of ΔT is ∼21 s, which results in a CPCP contribution of ∼7 kV. We have performed the same analysis for all large FTEs found in the six simulations, and found that the magnetic flux carried by individual large FTEs varies between 0.05 and 0.36 MWb, which is about 1.3%–11.9% of the total open flux in the polar cap. This result is in general agreement with the previous estimate of 8.8% obtained by Imber et al. (2014) through analysis of MESSENGER data. The contribution of individual large FTEs to the CPCP falls in the range between 4 and 29.8 kV in our simulation, which is also in line with the finding reached in previous studies based on MESSENGER observations (e.g., Imber et al., 2014; Slavin, Lepping, et al., 2010). The percentage contribution of a large FTE to the CPCP is about 7%–47.6%, which is consistent with the results reported in Sun, Dewey, et al. (2022) that individual FTEs can contribute up to ∼40% of the CPCP. Overall, we find that the properties of large FTEs simulated by our MHD-AEPIC model agrees very well with the results obtained in previous studies based on in-situ observations. Comparing the six simulations using different upstream conditions further reveals that large FTEs tend to carry more magnetic flux when the solar wind M_A is smaller and/or when the IMF clock angle is smaller.

4.3. Comparison Between MHD-AEPIC and Hall-MHD Simulations

Finally, we discuss the effects of kinetic physics on the characteristics of both simulated FTEs and reconnection X-lines. As mentioned in Section 2.1, the upstream conditions employed in this work are the same as those used in our previous global Hall-MHD simulations (Li et al., 2023), allowing us to make a direct comparison of simulation results between coupled fluid-kinetic model (i.e., MHD-AEPIC) and pure Hall MHD code. Figure 13 shows a comparison of various FTE properties and CPCP simulated by MHD-AEPIC and Hall-MHD models. The horizontal axis in each panel corresponds to the IMF clock angle in decreasing order. As shown, the majority of the quantities of interest extracted from MHD-AEPIC and Hall-MHD simulations display similar dependencies on the upstream solar wind M_A and IMF clock angle, with only few exceptions in FTE size, traveling speed, and core field strength. Furthermore, the observed dependencies on the upstream conditions are consistent with the findings reported in the recent MESSENGER survey of FTE shower events at Mercury (Sun et al., 2020). For instance, the temporal spacing between FTEs increases with increasing M_A number and decreasing IMF clock angle in both MHD-AEPIC and Hall-MHD simulations. Consequently, the occurrence of FTEs is most frequent when $M_A = 2$ and IMF clock angle = 180°.

Having evaluated the overall trends of various quantities shown in Figure 13, we now discuss the similarities and differences between MHD-AEPIC and Hall-MHD shown in Figure 13. We first focus on the impact of kinetic physics on CPCP, FTE speed, spacing, and density. As illustrated in Figure 13g, the CPCP values modeled by MHD-AEPIC and Hall-MHD are nearly identical, suggesting that kinetic effects do not significantly alter the global coupling efficiency between the solar wind and the magnetosphere. However, some differences can be observed in other FTE characteristics between the Hall-MHD and MHD-AEPIC models. For example, under the same upstream driving, the FTE speeds in the MHD-AEPIC model are generally smaller compared to those in the Hall-MHD model. The relatively slower FTE speeds in the MHD-AEPIC model would imply that FTEs can stay for a longer period on the dayside magnetopause (e.g., some FTEs and X-lines last for more than 20 s as shown in Figure 6). The FTE spacing is, in general, larger in the MHD-AEPIC model in comparison with Hall-MHD, suggesting that the generation of new X-lines occurs less frequently in the PIC model. This observed difference in FTE spacing is consistent with the result that individual X-line's lifetime on the dayside magnetopause is longer in the PIC model. We note that this decrease in the occurrence rate of FTEs, as simulated by the embedded PIC model, has also been reported previously in simulations of Ganymede's magnetosphere (Zhou et al., 2020). The FTE density consistently exhibits higher values in MHD-AEPIC simulations, which may be attributed to the

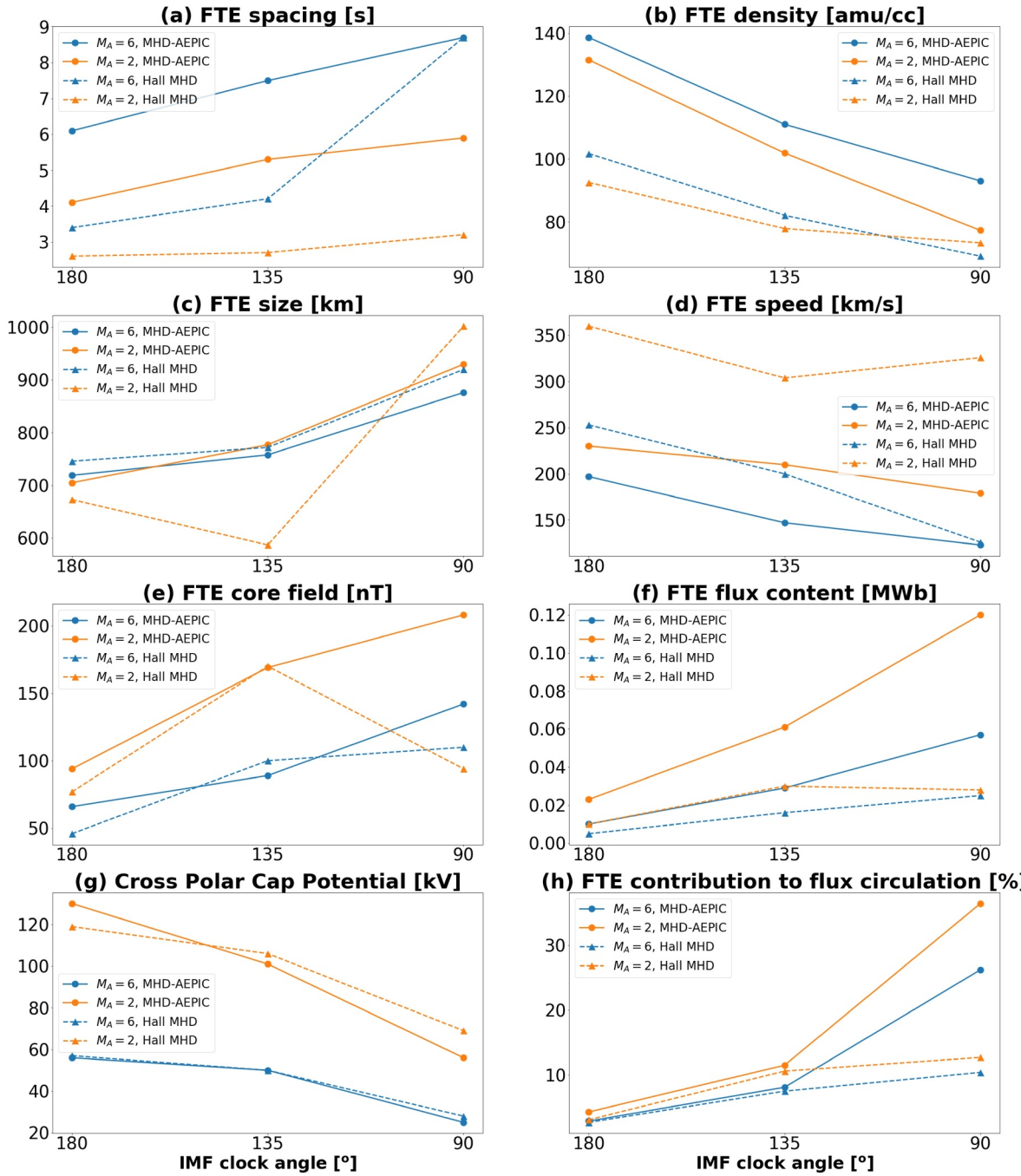

Figure 13. Comparison of various flux transfer event (FTE) properties and cross polar cap potential (CPCP) extracted from MHD-AEPIC and Hall-MHD simulations. The same set of upstream solar wind and interplanetary magnetic field (IMF) conditions were used as input to drive both models. The horizontal axis in each panel represents the IMF clock angles used in the simulations. The data points with the same M_A number are connected with solid and dashed lines for MHD-AEPIC and Hall-MHD simulations, respectively. The $M_A = 6$ simulations are represented by blue curves and the $M_A = 2$ simulations are indicated by orange curves. The quantities shown in panels (a)–(f) are FTE spacing, density, size, traveling speed, core field strength, magnetic flux content, CPCP, and FTEs' overall contribution to open flux generation, respectively.

result that the longer lifetime of FTE and reconnection X-line seen in the PIC model naturally lead to an increased injection of plasmas into the interior of FTE through reconnection outflow.

Next, we examine how the modeled FTE size, core field strength, magnetic flux content, and their overall contribution to open flux generation are affected when kinetic effects associated with reconnection are included in

the simulation. As shown by Figures 13c and 13e, the modeled FTE size and core field strength in the MHD-AEPIC simulations are, in general, very comparable to those seen in the Hall-MHD simulations using the same upstream conditions, with only a couple of exceptions. Particularly, in the $M_A = 2$ and IMF clock angle = 135° case, the average FTE size is smaller in Hall-MHD results, while for the case with $M_A = 2$ and IMF clock angle = 90°, the average FTE core field strength is lower in the Hall-MHD simulation compared to MHD-AEPIC simulation. In contrast, the average magnetic flux contents of FTE modeled by MHD-AEPIC are approximately twice those modeled by Hall-MHD under the same upstream driving. At a first glance, this discrepancy in FTE flux content seems to contradict with the result of comparable FTE size and core field strength observed in MHD-AEPIC and Hall-MHD simulations. However, our further analysis indicates that this result is due to the following two factors: (a) The standard deviations of the FTE size distribution in MHD-AEPIC simulations are smaller compared to Hall-MHD, suggesting that medium-size FTEs are more prevalent in MHD-AEPIC runs, and (b) the large-size FTEs seen in MHD-AEPIC tend to fall into the higher end of the core field strength distribution, resulting in well-formed FTEs carrying a substantial amount of open flux (which were termed as "large" FTEs previously in Section 4.2). We note that such correlation between large FTE size and strong core field is not seen in the Hall-MHD simulations. The FTE contribution (in the form of flux ropes) to open flux generation in the MHD-AEPIC simulations shows a considerable increase when compared to Hall-MHD, especially for the 90° IMF clock angle case. In particular, for $M_A = 6$ and IMF clock angle = 90° cases, the FTE contribution is 26.2% in MHD-AEPIC and 10.4% in Hall-MHD, while for $M_A = 2$ and IMF clock angle = 90° cases, the corresponding values are 36.4% for MHD-AEPIC and 12.7% for Hall-MHD. The substantial increase in FTE contributions to open flux generation in the MHD-AEPIC model at 90° IMF clock angle may have resulted from the differences in the characteristics of the local reconnection as modeled by PIC and Hall-MHD.

5. Summary and Conclusions

Taking advantage of the recent development of coupled fluid-kinetic simulations, we have conducted a series of global simulations of Mercury's magnetosphere to investigate the kinetic signatures, dawn-dusk asymmetries, and FTEs associated with dayside magnetopause reconnection. For this study, we have utilized the MHD-AEPIC model (Y. Chen et al., 2023; Shou et al., 2021; X. Wang et al., 2022) coupled with a planetary interior model (Jia et al., 2015, 2019) to simulate Mercury's magnetosphere. A non-rectangular PIC region was used to cover the entire dayside magnetosphere where reconnection is expected to occur. Six simulations were performed to study how Mercury's magnetosphere responds to different upstream parameters, specifically focusing on the impact of the solar wind Alfvénic Mach number and the IMF clock angle. Below we summarize the key results from our simulations.

The application of a fully kinetic approach to treat both ions and electrons in the embedded PIC model unveils distinct features in the plasma phase space distributions that result from magnetopause reconnection at Mercury. In particular, our results reveal crescent-shaped phase space distributions for both ions and electrons on the magnetosheath side of the reconnection sites. Additionally, near reconnection sites, electron phase space distributions exhibit signatures of preferential heating along the magnetic field direction, aligning with the reconnection outflow direction. In the cusp region, ion distributions exhibit counter-streaming behavior with two populations traveling in opposite directions relative to the magnetic field. Inside the FTEs, both ion and electron distributions are found to deviate from a Maxwellian distribution, showing notable signatures of temperature anisotropies due to magnetopause reconnection.

In all six simulations, where the upstream solar wind and IMF conditions are maintained at constant values, Mercury's magnetopause reconnection is found to occur in a non-steady manner resulting in FTEs with flux-rope like magnetic topology. In order to identify the reconnection X-lines in the 3D simulations, we have explored various published metrics used in studying reconnection physics, and have come up with a synthesized reconnection score, S, based on four reconnection metrics that works reasonably well for all of our simulations in identifying the locations of X-lines. By projecting the identified reconnection sites onto the MLT-latitude coordinates, we found that the distribution of reconnection occurrence at Mercury's dayside magnetopause exhibits significant dawn-dusk asymmetries in all six simulations, with the probability of reconnection events occurring on the dawnside ranging from 56% to 72%. The dawn-dusk asymmetry appears to be more pronounced in simulations with lower solar wind M_A and smaller IMF clock angle (or equivalently, IMF with larger B_y component). Potential processes that may have contributed to the dawn-dusk asymmetry seen in our simulations

include X-line spreading preferentially toward the dawn side due to the large flow speeds associated with the current-carrying electrons and suppression of reconnection on the dusk side due to the Hall effects in 3D reconnection.

An automated algorithm previously developed by Li et al. (2023) has been used to identify the large number of FTEs in the MHD-AEPIC simulations. The simulated FTEs are found to form frequently in our simulations with occurrence rates ranging from 4 to 9 s. Key properties of the FTEs, including their density, size, traveling speed, core field strength, and magnetic flux content were extracted from the simulations and compared with the results extracted from previous Hall-MHD simulations, which were driven by the same set of upstream conditions listed in Table 1. In both MHD-AEPIC and Hall-MHD simulations, the properties of simulated FTEs generally exhibit the same dependencies on the solar wind M_A and IMF clock angle, and the observed dependencies are consistent with the findings reported in previous observational studies based on MESSENGER data (e.g., Sun et al., 2020; Sun, Slavin, et al., 2022). However, some characteristics of FTEs seen in the MHD-AEPIC simulations differ from those in the Hall-MHD simulations, likely due to kinetic effects that are absent in the Hall-MHD model. Specifically, the FTEs and their associated reconnection X-lines, as modeled by PIC, tend to stay for a longer period of time on the magnetopause surface compared to their counterparts in Hall-MHD. The longer lifetime of FTEs and X-lines leads to slower FTE traveling speeds, slightly less frequent FTE occurrence, and higher FTE densities in the MHD-AEPIC model. The average magnetic flux content carried by FTEs simulated by MHD-AEPIC is approximately twice as high as those modeled by Hall-MHD, primarily due to the formation of greater number of "large" FTEs in the MHD-AEPIC simulation. These "large" FTEs in the MHD-AEPIC simulations carry about 1.3%–11.9% of the total polar cap flux and contribute 7%–47.6% of the average CPCP, which confirms the finding from previous MESSENGER work (e.g., Imber et al., 2014) that they play an important role in driving the global convection and dynamics in Mercury's magnetosphere.

In summary, we have employed a coupled fluid-kinetic model to investigate several aspects of reconnection-driven dynamics in Mercury's magnetosphere, including the kinetic signatures observed in particle distributions, the dawn-dusk asymmetry of reconnection occurrence on the dayside, and the formation and evolution of FTEs as captured by a fully kinetic model. The findings obtained through our simulations are expected to be useful for the interpretation of in situ measurements acquired by spacecraft missions, such as MESSENGER and BepiColombo, the latter scheduled to arrive at Mercury in late 2025 (Milillo et al., 2020).

It should be noted that the simulations presented in this work were conducted with idealized upstream conditions. One of the assumptions made in designing the model inputs was to neglect the radial component of the IMF, which would lead to additional north-south asymmetries in the global magnetospheric configuration and potentially influence characteristics of magnetopause reconnection, such as the primary X-line location on the magnetopause. Future work to incorporate more realistic IMF conditions into the simulation should be carried out to examine how the properties of Mercury's magnetopause reconnection and resultant FTEs are affected by the radial component of the IMF.

Appendix A: Nongyrotropy Measures

The two nongyrotropy measures presented in this study are both scalar quantities that are invariant with respect to the coordinate system. These measures can be computed locally on each grid point of the PIC model using the following equations. It is important to note that in the following equations the electron subscripts have been omitted in the expressions of the pressure tensor.

The first measure $A\varnothing$ is defined as

$$\mathbf{A}\varnothing = 2\frac{|\mathrm{P}_{\perp 1} - \mathrm{P}_{\perp 2}|}{\mathrm{P}_{\perp 1} + \mathrm{P}_{\perp 2}}, \tag{A1}$$

where the subscripts 1 and 2 represent the two directions perpendicular to the magnetic field. Scudder and Daughton (2008) showed that in any coordinate system (XYZ), one can define

$$\mathrm{N}_{xx} = b_y b_y P_{zz} - 2 b_y b_z P_{yz} + b_z b_z P_{yy}$$

$$N_{xy} = -b_y b_x P_{zz} + b_y b_z P_{xz} + b_z b_x P_{yz} - b_z b_z P_{xy}$$

$$N_{xz} = b_y b_x P_{yz} - b_y b_y P_{xz} - b_z b_x P_{yy} + b_z b_y P_{xy}$$

$$N_{yy} = b_x b_x P_{zz} - 2 b_x b_z P_{xz} + b_z b_z P_{xx}$$

$$N_{yz} = -b_x b_x P_{yz} + b_x b_y P_{xz} + b_z b_x P_{xy} - b_z b_y P_{xx}$$

$$N_{zz} = b_x b_x P_{yy} - 2 b_x b_y P_{xy} + b_y b_y P_{xx}$$

and

$$\alpha = N_{xx} + N_{yy} + N_{zz}$$

$$\beta = -\left(N_{xy}^2 + N_{xz}^2 + N_{yz}^2 - N_{xx}N_{yy} - N_{xx}N_{zz} - N_{yy}N_{zz}\right)$$

to write $\boldsymbol{A}\varnothing$ as

$$\boldsymbol{A}\varnothing = 2\frac{\sqrt{\alpha^2 - 4\beta}}{\alpha} \tag{A2}$$

The second nongyrotropy measure $\boldsymbol{Q}$ proposed by Swisdak (2016) is defined as

$$\boldsymbol{Q} = 1 - 4\frac{I_2}{(I_1 - P_{\parallel})(I_1 + 3P_{\parallel})} \tag{A3}$$

where $I_1 = P_{xx} + P_{yy} + P_{zz}$ is the trace of the electron pressure tensor and $I_2 = P_{xx}P_{yy} + P_{xx}P_{zz} + P_{yy}P_{zz} - (P_{xy}P_{yx} + P_{xz}P_{zx} + P_{yz}P_{zy})$ is the principle minor of the electron pressure tensor.

Data Availability Statement

The BATSRUS MHD code and the FLEKS code are publicly available for download as components of the SWMF at the University of Michigan (http://clasp.engin.umich.edu/swmf).

Acknowledgments
This work was supported by NASA Future Investigators in Earth and Space Science and Technology (FINESST) Grant 80NSSC1364, NASA Early Career Fellow startup Grant 80NSSC20K1286, and NASA Discovery Data Analysis Program through Grant 80NSSC21K1012. J. A. Slavin acknowledges support from NASA Grant 80NSSC21K0052. G. Toth was supported by the NSF PREEVENTS Grant 1663800. High-performance computing resources supporting this work were provided by NASA's High-End Computing Program through its Advanced Supercomputing (NAS) Division at Ames Research Center.

References

Akhavan-Tafti, M., Slavin, J. A., Eastwood, J. P., Cassak, P. A., & Gershman, D. J. (2019). MMS multi-point analysis of FTE evolution: Physical characteristics and dynamics. *Journal of Geophysical Research: Space Physics*, *124*(7), 5376–5395. https://doi.org/10.1029/2018JA026311

Akhavan-Tafti, M., Slavin, J. A., Sun, W. J., Le, G., & Gershman, D. J. (2019). MMS observations of plasma heating associated with FTE growth. *Geophysical Research Letters*, *46*(22), 12654–12664. https://doi.org/10.1029/2019GL084843

Anderson, B. J., Acuna, M. H., Korth, H., Purucker, M. E., Johnson, C. L., Slavin, J. A., et al. (2008). The structure of Mercury's magnetic field from MESSENGER's first flyby. *Science*, *321*(5885), 82–85. https://doi.org/10.1126/science.1159081

Anderson, B. J., Johnson, C. L., Korth, H., Purucker, M. E., Winslow, R. M., Slavin, J. A., et al. (2011). The global magnetic field of mercury from MESSENGER orbital observations. *Science*, *333*(6051), 1859–1862. https://doi.org/10.1126/science.1211001

Artemyev, A. V., Petrukovich, A. A., Nakamura, R., & Zelenyi, L. M. (2010). Proton velocity distribution in thin current sheets: Cluster observations and theory of transient trajectories. *Journal of Geophysical Research*, *115*(A12), A12255. https://doi.org/10.1029/2010JA015702

Baker, D. N., Pulkkinen, T. I., Angelopoulos, V., Baumjohann, W., & McPherron, R. L. (1996). Neutral line model of substorms: Past results and present view. *Journal of Geophysical Research*, *101*(A6), 12975–13010. https://doi.org/10.1029/95JA03753

Bessho, N., Chen, L.-J., Hesse, M., & Wang, S. (2017). The effect of reconnection electric field on crescent and U-shaped distribution functions in asymmetric reconnection with no guide field. *Physics of Plasmas*, *24*(7), 072903. https://doi.org/10.1063/1.4989737

Buchner, J., & Zelenyi, L. M. (1989). Regular and chaotic charged particle motion in magnetotaillike field reversals: 1. Basic theory of trapped motion. *Journal of Geophysical Research*, *94*(A9), 11821–11842. https://doi.org/10.1029/JA094iA09p11821

Burch, J. L., Torbert, R. B., Phan, T. D., Chen, L.-J., Moore, T. E., Ergun, R. E., et al. (2016). Electron-scale measurements of magnetic reconnection in space. *Science*, *352*(6290), aaf2939. https://doi.org/10.1126/science.aaf2939

Chen, J., & Palmadesso, P. J. (1986). Chaos and nonlinear dynamics of single-particle orbits in a magnetotaillike magnetic field. *Journal of Geophysical Research*, *91*(A2), 1499–1508. https://doi.org/10.1029/JA091iA02p01499

Chen, Y., & Tóth, G. (2019). Gauss's Law satisfying energy-conserving semi-implicit particle-in-cell method. *Journal of Computational Physics*, *386*, 632–652. https://doi.org/10.1016/j.jcp.2019.02.032

Chen, Y., Tóth, G., Cassak, P., Jia, X., Gombosi, T. I., Slavin, J. A., et al. (2017). Global three-dimensional simulation of Earth's dayside reconnection using a two-way coupled magnetohydrodynamics with embedded particle-in-cell model: Initial results. *Journal of Geophysical Research: Space Physics*, *122*(10), 10318–10335. https://doi.org/10.1002/2017JA024186

Chen, Y., Tóth, G., Jia, X., Slavin, J. A., Sun, W., Markidis, S., et al. (2019). Studying dawn-dusk asymmetries of Mercury's magnetotail using MHD-EPIC simulations. *Journal of Geophysical Research: Space Physics*, *124*(11), 8954–8973. https://doi.org/10.1029/2019JA026840

Chen, Y., Tóth, G., Zhou, H., & Wang, X. (2023). FLEKS: A flexible particle-in-cell code for multi-scale plasma simulations. *Computer Physics Communications*, *287*, 108714. https://doi.org/10.1016/j.cpc.2023.108714

Daldorff, L. K., Tóth, G., Gombosi, T. I., Lapenta, G., Amaya, J., Markidis, S., & Brackbill, J. U. (2014). Two-way coupling of a global Hall magnetohydrodynamics model with a local implicit particle-in-cell model. *Journal of Computational Physics*, *268*, 236–254. https://doi.org/10.1016/j.jcp.2014.03.009

DiBraccio, G. A., Slavin, J. A., Boardsen, S. A., Anderson, B. J., Korth, H., Zurbuchen, T. H., et al. (2013). MESSENGER observations of magnetopause structure and dynamics at Mercury. *Journal of Geophysical Research: Space Physics*, *118*(3), 997–1008. https://doi.org/10.1002/jgra.50123

Exner, W., Heyner, D., Liuzzo, L., Motschmann, U., Shiota, D., Kusano, K., & Shibayama, T. (2018). Coronal mass ejection hits Mercury: A.I.K. E.F. Hybrid-code results compared to MESSENGER data. *Planetary and Space Science*, *153*, 89–99. https://doi.org/10.1016/j.pss.2017.12.016

Fatemi, S., Poirier, N., Holmström, M., Lindkvist, J., Wieser, M., & Barabash, S. (2018). A modelling approach to infer the solar wind dynamic pressure from magnetic field observations inside Mercury's magnetosphere. *Astronomy and Astrophysics*, *614*, A132. https://doi.org/10.1051/0004-6361/201832764

Fear, R. C., Coxon, J. C., & Jackman, C. M. (2019). The contribution of flux transfer events to Mercury's Dungey cycle. *Geophysical Research Letters*, *46*(24), 14239–14246. https://doi.org/10.1029/2019GL085399

Gershman, D. J., Slavin, J. A., Raines, J. M., Zurbuchen, T. H., Anderson, B. J., Korth, H., et al. (2013). Magnetic flux pileup and plasma depletion in Mercury's subsolar magnetosheath. *Journal of Geophysical Research: Space Physics*, *118*(11), 7181–7199. https://doi.org/10.1002/2013JA019244

Gombosi, T. I., Chen, Y., Glocer, A., Huang, Z., Jia, X., Liemohn, M. W., et al. (2021). What sustained multi-disciplinary research can achieve: The space weather modeling framework. *Journal of Space Weather and Space Climate*, *11*, 42. https://doi.org/10.1051/swsc/2021020

Hesse, M., Aunai, N., Sibeck, D., & Birn, J. (2014). On the electron diffusion region in planar, asymmetric, systems. *Geophysical Research Letters*, *41*(24), 8673–8680. https://doi.org/10.1002/2014GL061586

Hwang, K.-J., Nakamura, R., Eastwood, J. P., Fuselier, S. A., Hasegawa, H., Nakamura, T., et al. (2023). Cross-scale processes of magnetic reconnection. *Space Science Reviews*, *219*(8), 71. https://doi.org/10.1007/s11214-023-01010-9

Imber, S. M., Slavin, J. A., Boardsen, S. A., Anderson, B. J., Korth, H., McNutt, R. L., & Solomon, S. C. (2014). MESSENGER observations of large dayside flux transfer events: Do they drive Mercury's substorm cycle? *Journal of Geophysical Research: Space Physics*, *119*(7), 5613–5623. https://doi.org/10.1002/2014JA019884

Jia, X., Slavin, J. A., Gombosi, T. I., Daldorff, L. K. S., Toth, G., & van der Holst, B. (2015). Global MHD simulations of Mercury's magnetosphere with coupled planetary interior: Induction effect of the planetary conducting core on the global interaction. *Journal of Geophysical Research: Space Physics*, *120*(6), 4763–4775. https://doi.org/10.1002/2015JA021143

Jia, X., Slavin, J. A., Poh, G., DiBraccio, G. A., Toth, G., Chen, Y., et al. (2019). MESSENGER observations and global simulations of highly compressed magnetosphere events at Mercury. *Journal of Geophysical Research: Space Physics*, *124*(1), 229–247. https://doi.org/10.1029/2018JA026166

Kieokaew, R., Lavraud, B., Fargette, N., Marchaudon, A., Génot, V., Jacquey, C., et al. (2021). Statistical relationship between interplanetary magnetic field conditions and the helicity sign of flux transfer event flux ropes. *Geophysical Research Letters*, *48*(6), e2020GL091257. https://doi.org/10.1029/2020GL091257

Lapenta, G. (2021). Detecting reconnection sites using the Lorentz transformations for electromagnetic fields. *The Astrophysical Journal*, *911*(2), 147. https://doi.org/10.3847/1538-4357/abeb74

Lapenta, G., Berchem, J., Zhou, M., Walker, R. J., El-Alaoui, M., Goldstein, M. L., et al. (2017). On the origin of the crescent-shaped distributions observed by MMS at the magnetopause. *Journal of Geophysical Research*, *122*(2), 2024–2039. https://doi.org/10.1002/2016JA023290

Lapenta, G., Schriver, D., Walker, R. J., Berchem, J., Echterling, N. F., El Alaoui, M., & Travnicek, P. (2022). Do we need to consider electrons' kinetic effects to properly model a planetary magnetosphere: The case of Mercury. *Journal of Geophysical Research: Space Physics*, *127*(4), e2021JA030241. https://doi.org/10.1029/2021JA030241

Lavorenti, F., Henri, P., Califano, F., Deca, J., Aizawa, S., André, N., & Benkhoff, J. (2022). Electron dynamics in small magnetospheres-Insights from global, fully kinetic plasma simulations of the planet Mercury. *Astronomy & Astrophysics*, *664*, A133. https://doi.org/10.1051/0004-6361/202243911

Lee, L. C., & Fu, Z. F. (1985). A theory of magnetic flux transfer at the Earth's magnetopause. *Geophysical Research Letters*, *12*(2), 105–108. https://doi.org/10.1029/GL012i002p00105

Li, C., Jia, X., Chen, Y., Toth, G., Zhou, H., Slavin, J. A., et al. (2023). Global Hall MHD simulations of Mercury's magnetopause dynamics and FTEs under different solar wind and IMF conditions. *Journal of Geophysical Research: Space Physics*, *128*(5), e2022JA031206. https://doi.org/10.1029/2022JA031206

Liu, Y.-H., Li, T. C., Hesse, M., Sun, W. J., Liu, J., Burch, J., et al. (2019). Three-dimensional magnetic reconnection with a spatially confined X-line extent: Implications for dipolarizing flux bundles and the dawn-dusk asymmetry. *Journal of Geophysical Research: Space Physics*, *124*(4), 2819–2830. https://doi.org/10.1029/2019JA026539

Lottermoser, R.-F., Scholer, M., & Matthews, A. P. (1998). Ion kinetic effects in magnetic reconnection: Hybrid simulations. *Journal of Geophysical Research*, *103*(A3), 4547–4559. https://doi.org/10.1029/97ja01872

Lu, Q., Guo, J., Lu, S., Wang, X., Slavin, J. A., Sun, W., et al. (2022). Three-dimensional global hybrid simulations of flux transfer event showers at Mercury. *The Astrophysical Journal*, *937*(1), 1. https://doi.org/10.3847/1538-4357/ac8bcf

Milillo, A., Fujimoto, M., Murakami, G., Benkhoff, J., Zender, J., Aizawa, S., et al. (2020). Investigating Mercury's environment with the two-spacecraft BepiColombo mission. *Space Science Reviews*, *216*(5), 1–78. https://doi.org/10.1007/s11214-020-00712-8

Müller, J., Simon, S., Wang, Y. C., Motschmann, U., Heyner, D., Schüle, J., et al. (2012). Origin of Mercury's double magnetopause: 3D hybrid simulation study with A.I.K.E.F. *Icarus*, *218*(1), 666–687. https://doi.org/10.1016/j.icarus.2011.12.028

Nakamura, T. K. M., Nakamura, R., Alexandrova, A., Kubota, Y., & Nagai, T. (2012). Hall magnetohydrodynamic effects for three-dimensional magnetic reconnection with finite width along the direction of the current. *Journal of Geophysical Research*, *117*(A3), A03220. https://doi.org/10.1029/2011JA017006

Poh, G., Slavin, J. A., Jia, X., Raines, J. M., Imber, S. M., Sun, W.-J., et al. (2017). Coupling between Mercury and its nightside magnetosphere: Cross-tail current sheet asymmetry and substorm current wedge formation. *Journal of Geophysical Research: Space Physics*, *122*(8), 8419–8433. https://doi.org/10.1002/2017JA024266

Powell, K. G., Roe, P. L., Linde, T. J., Gombosi, T. I., & De Zeeuw, D. L. (1999). A solution-adaptive upwind scheme for ideal magnetohydrodynamics. *Journal of Computational Physics*, *154*(2), 284–309. https://doi.org/10.1006/jcph.1999.6299

Rijnbeek, R. P., Cowley, S. W. H., Southwood, D. J., & Russell, C. T. (1984). A survey of dayside flux transfer events observed by ISEE 1 and 2 magnetometers. *Journal of Geophysical Research*, *89*(A2), 786–800. https://doi.org/10.1029/ja089ia02p00786

Russell, C. T., & Elphic, R. C. (1978). Initial ISEE magnetometer results: Magnetopause observations. *Space Science Reviews*, *22*(6), 681–715. https://doi.org/10.1007/BF00212619

Russell, C. T., Le, G., & Kuo, H. (1996). The occurrence rate of flux transfer events. *Advances in Space Research*, *18*(8), 197–205. https://doi.org/10.1016/0273-1177(95)00965-5

Schindler, K., Hesse, M., & Birn, J. (1988). General magnetic reconnection, parallel electric fields, and helicity. *Journal of Geophysical Research*, *93*(A6), 5547–5557. https://doi.org/10.1029/JA093iA06p05547

Scholer, M. (1988). Magnetic flux transfer at the magnetopause based on single X line bursty reconnection. *Geophysical Research Letters*, *15*(4), 291–294. https://doi.org/10.1029/GL015i004p00291

Scudder, J., & Daughton, W. (2008). Illuminating electron diffusion regions of collisionless magnetic reconnection using electron agyrotropy. *Journal of Geophysical Research*, *113*(A6), A06222. https://doi.org/10.1029/2008JA013035

Shay, M. A., Phan, T. D., Haggerty, C. C., Fujimoto, M., Drake, J. F., Malakit, K., et al. (2016). Kinetic signatures of the region surrounding the X line in asymmetric (magnetopause) reconnection. *Geophysical Research Letters*, *43*(9), 4145–4154. https://doi.org/10.1002/2016GL069034

Shepherd, L. S., & Cassak, P. A. (2012). Guide field dependence of 3-D X-line spreading during collisionless magnetic reconnection. *Journal of Geophysical Research*, *117*(A10), A10101. https://doi.org/10.1029/2012JA017867

Shou, Y., Tenishev, V., Chen, Y., Toth, G., & Ganushkina, N. (2021). Magnetohydrodynamic with adaptively embedded particle-in-cell model: MHD-AEPIC. *Journal of Computational Physics*, *446*, 110656. https://doi.org/10.1016/j.jcp.2021.110656

Shue, J.-H., Chao, J. K., Fu, H. C., Russell, C. T., Song, P., Khurana, K. K., & Singer, H. J. (1997). A new functional form to study the solar wind control of the magnetopause size and shape. *Journal of Geophysical Research*, *102*(A5), 9497–9511. https://doi.org/10.1029/97JA00196

Slavin, J. A., Acuña, M. H., Anderson, B. J., Baker, D. N., Benna, M., Boardsen, S. A., et al. (2009). MESSENGER observations of magnetic reconnection in Mercury's magnetosphere. *Science*, *324*(5927), 606–610. https://doi.org/10.1126/science.1172011

Slavin, J. A., Acuna, M. H., Anderson, B. J., Baker, D. N., Benna, M., Gloeckler, G., et al. (2008). Mercury's magnetosphere after MESSENGER's first flyby. *Science*, *321*(5885), 85–89. https://doi.org/10.1126/science.1159040

Slavin, J. A., Anderson, B. J., Baker, D. N., Benna, M., Boardsen, S. A., Gloeckler, G., et al. (2010). MESSENGER observations of extreme loading and unloading of Mercury's magnetic tail. *Science*, *329*(5992), 665–668. https://doi.org/10.1126/science.1188067

Slavin, J. A., & Holzer, R. E. (1979). The effect of erosion on the solar wind stand-off distance at Mercury. *Journal of Geophysical Research*, *84*(A5), 2076–2082. https://doi.org/10.1029/JA084iA05p02076

Slavin, J. A., Imber, S. M., Boardsen, S. A., DiBraccio, G. A., Sundberg, T., Sarantos, M., et al. (2012). MESSENGER observations of a flux-transfer-event shower at Mercury. *Journal of Geophysical Research*, *117*(A12), A00M06. https://doi.org/10.1029/2012JA017926

Slavin, J. A., Lepping, R. P., Wu, C.-C., Anderson, B. J., Baker, D. N., Benna, M., et al. (2010). MESSENGER observations of large flux transfer events at Mercury. *Geophysical Research Letters*, *37*(2), L02105. https://doi.org/10.1029/2009GL041485

Southwood, D. J., Farrugia, C. J., & Saunders, M. A. (1988). What are flux transfer events? *Planetary and Space Science*, *36*(5), 503–508. https://doi.org/10.1016/0032-0633(88)90109-2

Sun, W., Dewey, R. M., Aizawa, S., Huang, J., Slavin, J. A., Fu, S., et al. (2022). Review of Mercury's dynamic magnetosphere: Post-MESSENGER era and comparative magnetospheres. *Science China Earth Sciences*, *65*(1), 25–74. https://doi.org/10.1007/s11430-021-9828-0

Sun, W., Slavin, J. A., Milillo, A., Dewey, R. M., Orsini, S., Jia, X., et al. (2022). MESSENGER observations of planetary ion enhancements at Mercury's northern magnetospheric cusp during flux transfer event showers. *Journal of Geophysical Research: Space Physics*, *127*(4), e2022JA030280. https://doi.org/10.1029/2022JA030280

Sun, W. J., Fu, S. Y., Slavin, J. A., Raines, J. M., Zong, Q. G., Poh, G. K., & Zurbuchen, T. H. (2016). Spatial distribution of Mercury's flux ropes and reconnection fronts: MESSENGER observations. *Journal of Geophysical Research: Space Physics*, *121*(8), 7590–7607. https://doi.org/10.1002/2016JA022787

Sun, W. J., Slavin, J. A., Smith, A. W., Dewey, R. M., Poh, G. K., Jia, X., et al. (2020). Flux transfer event showers at Mercury: Dependence on plasma β and magnetic shear and their contribution to the Dungey cycle. *Geophysical Research Letters*, *47*(21), e2020GL089784. https://doi.org/10.1029/2020GL089784

Swisdak, M. (2016). Quantifying gyrotropy in magnetic reconnection. *Geophysical Research Letters*, *43*(1), 43–49. https://doi.org/10.1002/2015GL066980

Swisdak, M., Opher, M., Drake, J. F., & Alouani Bibi, F. (2010). The vector direction of the interstellar magnetic field outside the heliosphere. *The Astrophysical Journal*, *710*(2), 1769–1775. https://doi.org/10.1088/0004-637x/710/2/1769

Tóth, G., Chen, Y., Gombosi, T. I., Cassak, P., Markidis, S., & Peng, I. B. (2017). Scaling the ion inertial length and its implications for modeling reconnection in global simulations. *Journal of Geophysical Research: Space Physics*, *122*(10), 10336–10355. https://doi.org/10.1002/2017JA024189

Tóth, G., Jia, X., Markidis, S., Peng, I. B., Chen, Y., Daldorff, L. K. S., et al. (2016). Extended magnetohydrodynamics with embedded particle-in-cell simulation of Ganymede's magnetosphere. *Journal of Geophysical Research: Space Physics*, *121*(2), 1273–1293. https://doi.org/10.1002/2015JA021997

Tóth, G., Ma, Y., & Gombosi, T. I. (2008). Hall magnetohydrodynamics on block-adaptive grids. *Journal of Computational Physics*, *227*(14), 6967–6984. https://doi.org/10.1016/j.jcp.2008.04.010

Tóth, G., Van der Holst, B., Sokolov, I. V., De Zeeuw, D. L., Gombosi, T. I., Fang, F., et al. (2012). Adaptive numerical algorithms in space weather modeling. *Journal of Computational Physics*, *231*(3), 870–903. https://doi.org/10.1016/j.jcp.2011.02.006

Trávníček, P. M., Schriver, D., Hellinger, P., Herˇcík, D., Anderson, B. J., Sarantos, M., & Slavin, J. A. (2010). Mercury's magnetosphere-solar wind interaction for northward and southward interplanetary magnetic field: Hybrid simulation results. *Icarus*, *209*(1), 11–22. https://doi.org/10.1016/j.icarus.2010.01.008

Wang, S., Kistler, L. M., Mouikis, C. G., Liu, Y., & Genestreti, K. J. (2014). Hot magnetospheric O^+ and cold ion behavior in magnetopause reconnection: Cluster observations. *Journal of Geophysical Research: Space Physics*, *119*(12), 9601–9623. https://doi.org/10.1002/2014JA020402

Wang, X., Chen, Y., & Tóth, G. (2022). Global magnetohydrodynamic magnetosphere simulation with an adaptively embedded particle-in-cell model. *Journal of Geophysical Research: Space Physics*, *127*(8), e2021JA030091. https://doi.org/10.1029/2021JA030091

Winslow, R. M., Anderson, B. J., Johnson, C. L., Slavin, J. A., Korth, H., Purucker, M. E., et al. (2013). Mercury's magnetopause and bow shock from MESSENGER Magnetometer observations. *Journal of Geophysical Research: Space Physics*, *118*(5), 2213–2227. https://doi.org/10.1002/jgra.50237

Zenitani, S., Hesse, M., Klimas, A., & Kuznetsova, M. (2011). New measure of the dissipation region in collisionless magnetic reconnection. *Physical Review Letters*, *106*(19), 195003. https://doi.org/10.1103/PhysRevLett.106.195003

Zhou, H., Tóth, G., Jia, X., & Chen, Y. (2020). Reconnection-driven dynamics at Ganymede's upstream magnetosphere: 3-D global Hall MHD and MHD-EPIC simulations. *Journal of Geophysical Research: Space Physics*, *125*(8), e2020JA028162. https://doi.org/10.1029/2020JA028162

Zhou, H., Tóth, G., Jia, X., Chen, Y., & Markidis, S. (2019). Embedded kinetic simulation of Ganymede's magnetosphere: Improvements and inferences. *Journal of Geophysical Research: Space Physics*, *124*(7), 5441–5460. https://doi.org/10.1029/2019JA026643

Zou, Y., Walsh, B. M., Nishimura, Y., Angelopoulos, V., Ruohoniemi, J. M., McWilliams, K. A., & Nishitani, N. (2018). Spreading speed of magnetopause reconnection X-lines using ground-satellite coordination. *Geophysical Research Letters*, *45*(1), 80–89. https://doi.org/10.1002/2017GL075765

Zurbuchen, T. H., Raines, J. M., Slavin, J. A., Gershman, D. J., Gilbert, J. A., Gloeckler, G., et al. (2011). MESSENGER observations of the spatial distribution of planetary ions near Mercury. *Science*, *333*(6051), 1862–1865. https://doi.org/10.1126/science.1211302